論文 / 著書情報
Article / Book Information

Title	Marine magnetotelluric inversion with an unstructured tetrahedral mesh
Authors	Yoshiya Usui, Takafumi Kasaya, Yasuo Ogawa, Hisanori Iwamoto
Citation	Geophysical Journal International, Vol. 214, 2, p. 952－974
Pub. date	2018, 5
DOI	https://doi.org/10.1093/gji/ggy171
Copyright	This article has been accepted for publication in Geophysical Journal International (c): 2018Yoshiya Usui,Takafumi Kasaya,Yasuo Ogawa,Hisanori Iwamoto Published by Oxford University Press on behalf of Royal Astronomical Society. All rights reserved.

Geophysical Journal International

Geophys. J. Int. (2018) **214,** 952–974
Advance Access publication 2018 May 05
GJI Marine geosciences and applied geophysics

doi: 10.1093/gji/ggy171

Marine magnetotelluric inversion with an unstructured tetrahedral mesh

Yoshiya Usui,[1,2] Takafumi Kasaya,[3,4] Yasuo Ogawa[2] and Hisanori Iwamoto[4]

[1]*Department of Earth and Planetary Sciences, Tokyo Institute of Technology, Tokyo* 152-8551, *Japan. E-mail: yoshiya.usui@gmail.com*
[2]*Volcanic Fluid Research Center, Tokyo Institute of Technology, Tokyo* 152-8551, *Japan*
[3]*Research and Development Center for Earthquake and Tsunami, Japan Agency for Marine–Earth Science and Technology, Yokosuka, Kanagawa* 237-0061, *Japan*
[4]*Project Team for Development of New-generation Research Protocol for Submarine Resources, Japan Agency for Marine–Earth Science and Technology, Yokosuka, Kanagawa* 237-0061, *Japan*

Accepted 2018 April 27. Received 2018 April 14; in original form 2017 August 10

SUMMARY

The finite element method using an unstructured tetrahedral mesh is one of the most effective methods for the 3-D modelling of marine magnetotelluric data that are strongly affected by bathymetry, because it enables us to incorporate both small-scale and regional-scale bathymetry into a computational mesh with a practical number of elements. The authors applied a 3-D inversion scheme using mesh of this type to marine magnetotelluric problems for the first time and verified its applicability. Forward calculations for two bathymetry models demonstrated that the results obtained with an unstructured tetrahedral mesh are close to the reference solutions. To evaluate the forward calculation results, we developed a general TM-mode analytical formulation for a 2-D sinusoidal topography. Moreover, synthetic inversion test results confirmed that a 3-D inversion scheme with an unstructured tetrahedral mesh enables us to recover subseafloor resistivity structure properly even for a model including a land–sea boundary as well as seafloor undulations.

The verified inversion scheme was subsequently applied to a set of marine magnetotelluric data observed around the Iheya North Knoll, the middle Okinawa Trough. 3-D modelling using a mesh with precise bathymetry demonstrated that the data observed around the Iheya North Knoll are strongly affected by bathymetry, especially by the sea-depth differences between the depression of the trough and the shallow East China Sea. The estimated resistivity structure under the knoll is characterized by a conductive surface layer underlain by a resistive layer. The conductive layer implies permeable pelagic/hemipelagic sediments, which are consistent with a previous seismological study. Furthermore, the conductive layer has a resistive part immediately below the knoll, which is regarded as the consolidated magma intrusion that formed the knoll. Furthermore, at a depth of 10 km, we found that the resistor underneath the knoll extends to the southeast, implying that subseafloor resistivity under the Volcanic Arc Migration Phenomenon area is more resistive than the surroundings due to the presence of consolidated magma.

Key words: Electrical properties; Magnetotellurics; Marine electromagnetics; Inverse theory; Numerical modelling; Backarc basin processes.

1 INTRODUCTION

The effect of bathymetry has persisted as an extremely important issue in marine magnetotelluric (MT) modelling. Observation sites of marine MT surveys are located on undulating seafloor, which makes the electromagnetic (EM) field at the observation sites depart from that on a flat surface (e.g. Baba & Seama 2002; Schwalenberg & Edwards 2004; Key 2012). In addition, the land–sea boundary has a considerably strong

* Now at: Itochu Techno-Solutions Corp., 3-2-5, Kasumigaseki, Chiyoda-ku, Tokyo 100-6080, Japan.

effect on the EM field, even at distant seafloor areas (e.g. Key & Constable 2011; Worzewski *et al.* 2012). Therefore, unless these bathymetric effects are considered in the modelling phase, it is possible to misinterpret subseafloor resistivity structure.

To prevent the misinterpretation by diminishing the bathymetric effects, two different approaches have been proposed (Matsuno *et al.* 2007; Li *et al.* 2008; Key 2012): the correction method and the direct method. In the correction method, distortions due to bathymetry are estimated prior to MT inversion from the forward results using the grids with and without bathymetry, and then resistivity structure is inverted from the data preliminarily corrected to be free of the distortions using the grid without the bathymetry (e.g. Baba & Chave 2005; Matsuno *et al.* 2007). A number of correction equations, which describe the relation between the response function or EM field distorted by bathymetric effects and the undistorted ones, have been proposed (e.g. Nolasco *et al.* 1998; Baba & Chave 2005; Matsuno *et al.* 2007). For instance, Baba & Chave (2005) assumed the following equation to relate the distorted impedance tensor to the undistorted one as

$$\boldsymbol{Z} = \boldsymbol{C}\boldsymbol{Z}_m, \tag{1}$$

where $\boldsymbol{Z} \in \mathbb{C}^{2\times 2}$ is the impedance tensor affected by bathymetry, $\boldsymbol{C} \in \mathbb{C}^{2\times 2}$ is the tensor describing local bathymetric effects and $\boldsymbol{Z}_m \in \mathbb{C}^{2\times 2}$ is the impedance tensor free of the bathymetric effects. In the correction method, there is a merit of taking account of the bathymetric effects with less computational cost than the direct method since it requires a smaller number of grids than the direct method. However, if the correction equation (e.g. eq. 1) does not hold, the local bathymetric effects are not removed properly from observed data. Consequently, subseafloor resistivity structure can be misinterpreted. Key & Constable (2011) and Key (2012) insisted that the use of the correction method has proven effective only for long-period MT surveys in the deep ocean, where the bathymetric effect can be decoupled from the deep upper-mantle structure under investigation. Therefore, for some areas such as deep ocean basin and continental margin, they suggested that one must use the direct method rather than the correction method to estimate resistivity structure reliably.

In contrast to the correction method, the direct method requires no correction equations because it directly incorporates seafloor undulations and land–sea boundaries into a computational grid used in MT inversion to incorporate consideration of the bathymetric effects. The direct method is, therefore, more robust to various marine MT problems (Key 2012). Although the direct method has a disadvantage of requiring a larger computational load than the correction method, this disadvantage is no longer a significant problem because of the rapid increasing of computational resources in recent years.

In 2-D marine MT problems, several inversion schemes have been proposed to incorporate bathymetry directly into a numerical grid. Li *et al.* (2008) proposed an effective finite difference approximation to incorporate bathymetry into a numerical grid. Additionally, over the last decade, 2-D codes based on the finite element method (FEM) with a triangular unstructured mesh have been developed (e.g. Key & Weiss 2006; Li & Key 2007; Key 2016). FEM with an unstructured triangular mesh presents the benefit of incorporating complex-shaped seafloor undulations and coastlines into a computational mesh precisely and efficiently.

In recent years, 3-D marine MT simulations have been performed with the aid of increasing computational resources. In most 3-D marine MT modellings, the finite difference method (FDM) is used (e.g. Tada *et al.* 2014; Baba *et al.* 2016; Tada *et al.* 2016). When FDM is used, it is necessary to represent seafloor undulations and land–sea boundaries as a series of discrete jumps or stair steps. However, for 3-D marine MT problems, such a 'stair-case' method requires an impractically large number of numerical cells to incorporate the entire bathymetry into a computational grid (Constable *et al.* 2009; Baba *et al.* 2013). Therefore, no 3-D inversion scheme that can represent the entire bathymetry in one numerical grid with a practical number of degrees-of-freedom has been proposed (Constable *et al.* 2009; Utada 2015).

To avoid that difficulty, Baba *et al.* (2013) developed a two-stage modelling scheme for 3-D marine MT data. In that scheme, regional bathymetry is represented in a large numerical grid where local small-scale bathymetry is not incorporated while the effects of the small-scale bathymetry are evaluated using finer small-size grids located around each observation site. Those effects are considered by local bathymetric distortion terms [$\mathbf{D}^{\mathrm{lt}}$ of eq. (1) of Baba *et al.* (2013)], as in the correction method described above. In the inversion part of that scheme, the 3-D inversion scheme proposed by Tada *et al.* (2012) is used. However, it was reported that this approach can fail to provide the correct resistivity structure unless the prior and initial model closely approximate the actual resistivity structure (Baba *et al.* 2013). In addition to the nonlinear nature of MT inversion, the uses of the prior model and the local bathymetric distortion term, which is estimated from the initial model, are likely to make the inversion result dependent on the prior model and the initial model. Furthermore, the two-stage modelling scheme has been proven valid only for long-period MT soundings to image the deep upper-mantle structure up to a depth of several hundred kilometres.

As described above, in 2-D marine MT problems, FEM with an unstructured mesh has been used to incorporate bathymetry precisely and efficiently. Furthermore, in some other geoelectric and geomagnetic exploration methods, FEM using an unstructured tetrahedral mesh has been increasingly used for 3-D modelling owing to its capability of incorporating precise topography and bathymetry into a computational mesh with a practical number of elements (Günther *et al.* 2006; Schwarzbach & Haber 2013; Usui 2015). For 3-D land MT problem, Usui (2015) demonstrated that the approximation error of topographic expression can be reduced sufficiently by using an unstructured tetrahedral mesh, and Usui *et al.* (2017) estimated the 3-D resistivity structure of Asama Volcano with a data-space MT inversion code using mesh of that type. In addition, Schwarzbach & Haber (2013) demonstrated the applicability of an unstructured tetrahedral mesh to 3-D marine controlled source electromagnetics. Baba *et al.* (2013) also described that 3-D MT inversion using an unstructured mesh is probably a practical approach to incorporate both local-scale and regional-scale bathymetry into a computational mesh. By making fine elements only around the area where small-scale bathymetry must be represented precisely (e.g. around observation sites) and by keeping the other areas having larger elements, the unstructured tetrahedral mesh can prevent significant increase of the number of elements, even when both local-scale and regional-scale bathymetry are incorporated into a computational mesh.

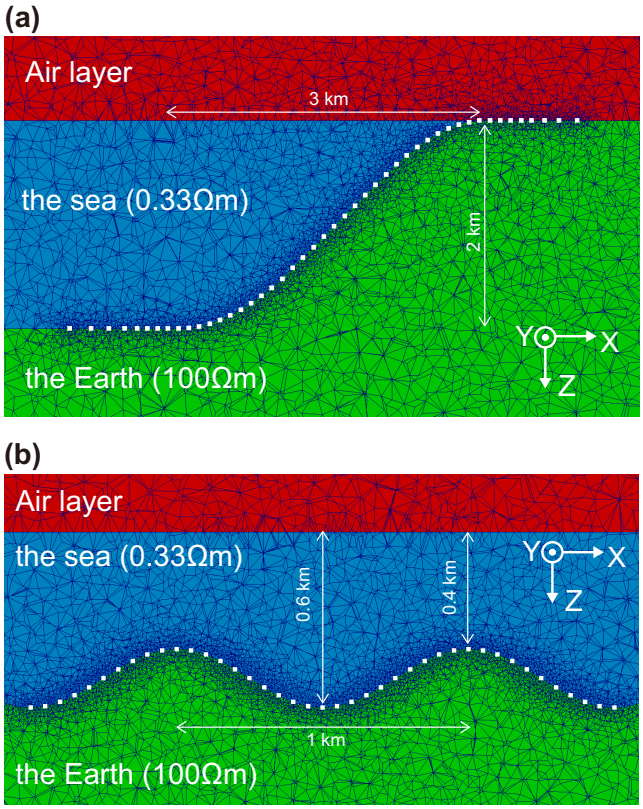

Figure 1. Cross-section of the computational meshes used for the forward calculations. (a) Bathymetry model of Li *et al.* (2008). (b) Bathymetry model of Schwalenberg & Edwards (2004). White dots on the seafloor denote the calculation points of the MT response functions.

However, in spite of the benefits explained above, unstructured tetrahedral mesh has not been used in 3-D marine MT problems. In this study, we therefore applied the inversion scheme of Usui (2015) to 3-D marine MT problems and verified its applicability. In addition to the capability to incorporate consideration of the bathymetric effect by an unstructured tetrahedral mesh, the inversion scheme presented by Usui (2015) prevents the inversion result from depending on the prior model because the regularization term of the inversion scheme of Usui (2015) does not force subsurface resistivity to be close to any prior model but just makes smaller the spatial changes of the subsurface resistivity to be estimated.

First, we will verify the forward calculation part of the inversion scheme of Usui (2015) using two models with bathymetry. After that, we apply the inversion scheme to a synthetic data that are affected by bathymetry to confirm that the scheme recovers subseafloor resistivity structure properly by incorporating the bathymetry into an unstructured tetrahedral mesh. Finally, we applied the inversion scheme to an actual data set observed around the Iheya North Knoll in the middle Okinawa Trough.

2 APPLICABILITY TEST OF THE UNSTRUCTURED TETRAHEDRAL MESH TO MARINE MT INVERSION

2.1 Verification of the forward calculation part

First, the authors will verify that the forward calculation part of the inversion scheme of Usui (2015) can provide accurate response functions at seafloor points of the model with bathymetry. Although many studies have investigated the effects of bathymetry on marine MT responses, the number of the studies showing comparable response functions is very limited, especially for 3-D problems. For that reason, we used two 2-D bathymetry models for the verification.

One of the models is the bathymetry model introduced by Li *et al.* (2008), with a steep seafloor slope having 3 km width and 2 km depth. The maximum slope of the model is 45°. Since Li *et al.* (2008) do not show the detail information about the bathymetry, the bathymetry was read from fig. 4 of Li *et al.* (2008). Li *et al.* (2008) calculated the TM-mode and TE-mode response functions at the periods of 100 and 1000 s using their scheme with a finite difference approximation. To calculate the marine MT response functions, the authors constructed an unstructured tetrahedral mesh with a bathymetry slope parallel to the *y*-direction (Fig. 1a) with the aid of TetGen (Si 2007). The size of the computational mesh is 1000 km × 1000 km × 1100 km. In the finest region near the observation points, edge lengths are forced to be approximately 30 m. The total number of elements is 815 363. The resistivities of the sea and the land parts were set, respectively, as 0.33 and 100 Ωm. As in Li *et al.* (2008), the tangential electric field and the horizontal magnetic field were used to calculate response functions.

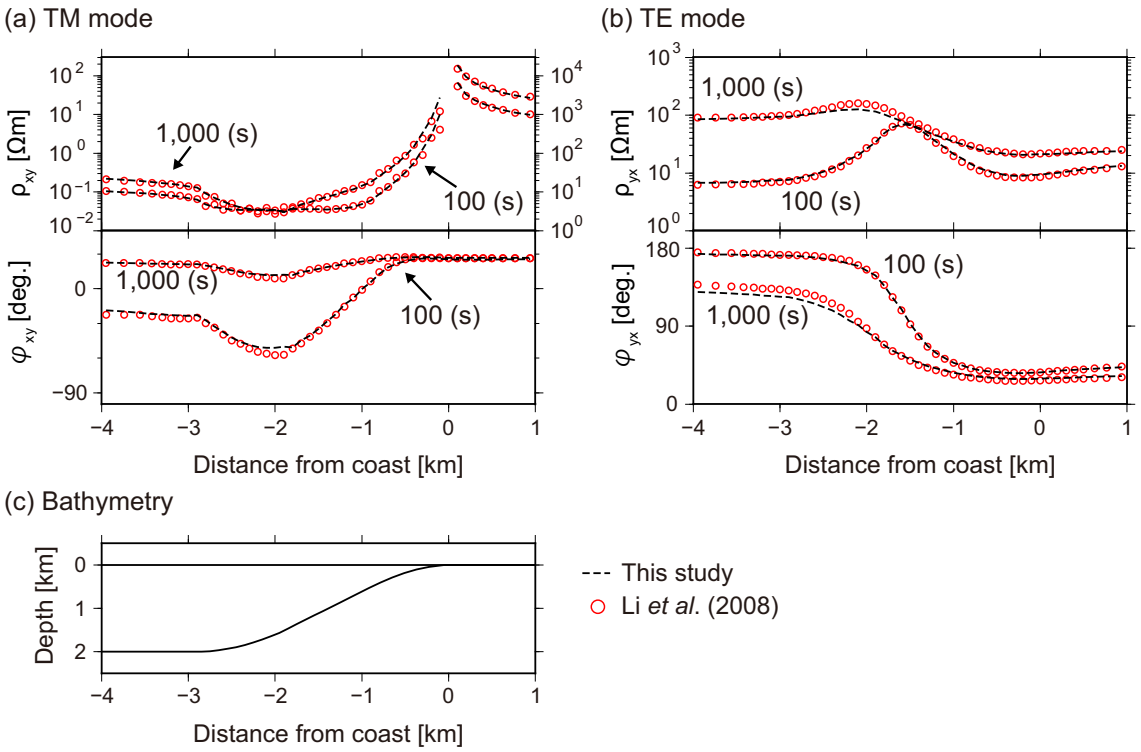

Figure 2. Comparison of the seafloor MT response functions calculated in this study with the results of Li *et al.* (2008). (a) TM-mode apparent resistivity and phase. (b) TE-mode apparent resistivity and phase. (c) Sea surface and seafloor topography.

The tangential electric field at the seafloor was interpolated from the electric field of the element edges on the seafloor. On the other hand, the horizontal magnetic field at the seafloor was calculated using the Faraday's law from the electric field of all edges of the element just below each observation site. The element under the seafloor was used because the change of the magnetic field is smaller in the subseafloor side than that in the sea.

For comparison, the calculated apparent resistivity and phase are presented with those of Li *et al.* (2008) in Fig. 2. The apparent resistivity and phase of the TE mode change markedly in the sea because of the electric current flowing intensively along the coast (Constable *et al.* 2009; Worzewski *et al.* 2012). On the other hand, the apparent resistivity of the TM mode changes discontinuously at the land–sea boundary. At the land side near the coast, the apparent resistivity increases by several orders of magnitude, probably because of the discontinuous electric field at the land–sea boundary resulting from the continuous current flow traversing the coast (Fischer 1979). However, at the ocean side, the galvanic ocean-side coast effect decreases the apparent resistivity observed at the seafloor by several orders of magnitude. Although the accuracy of the calculated response functions cannot be quantitatively assessed because the reading error of the bathymetry may cause some differences of the response functions, the solutions of this study are similar to those presented by Li *et al.* (2008).

The second model is the basic model used in Schwalenberg & Edwards (2004). The seafloor of the model has a sinusoidal undulation. As the electrical conductivities, the amplitude and the wavelength of the seafloor undulation, the authors adopted the values written in table 1 of Schwalenberg & Edwards (2004). The mesh used for forward calculation (Fig. 1b) was made with the aid of TetGen (Si 2007). The size of the computational mesh is 1000 km × 1000 km × 1100 km and the total number of elements is 1 149 048. The minimum edge length is about 10 m. Response functions of 100 and 1000 s were calculated at each observation site shown in Fig. 1(b). In calculating the response functions, the horizontal electric field and the horizontal magnetic field at the seafloor were used. The horizontal magnetic field at each site was calculated from the electric field of the subseafloor element as explained above. On the other hand, the horizontal electric field was interpolated from the electric field of all edges of the element just above each observation site. The electric field varies significantly across the seafloor since the normal component of the electric field is discontinuous due to the difference between the electrical conductivity of the sea and that of the subseafloor region. Thus, it is deemed appropriate to interpolate the electric field used in the marine MT modelling, which is observed above the seafloor, from the element above the seafloor. In all of the calculations described in the following sections, the same approach was used to calculate response functions of the observation sites on the seafloor.

The analytical formulation for a 2-D sinusoidal topography was proposed by Schwalenberg & Edwards (2004). However, in the TM-mode analytical formulation of Schwalenberg & Edwards (2004), the contributions of the vertical electric field to the tangential electric field on the interface between the upper region and the lower region are neglected, and it is assumed that the horizontal electric component, instead of the tangential component, is continuous across the interface. For undulating seafloor, this approximation seems to cause significant error to the analytical solution since the normal component of the electric field below the seafloor is much greater than that above the seafloor due to the continuity of the normal component of the electric current and significantly higher electrical conductivity in the sea compared to that

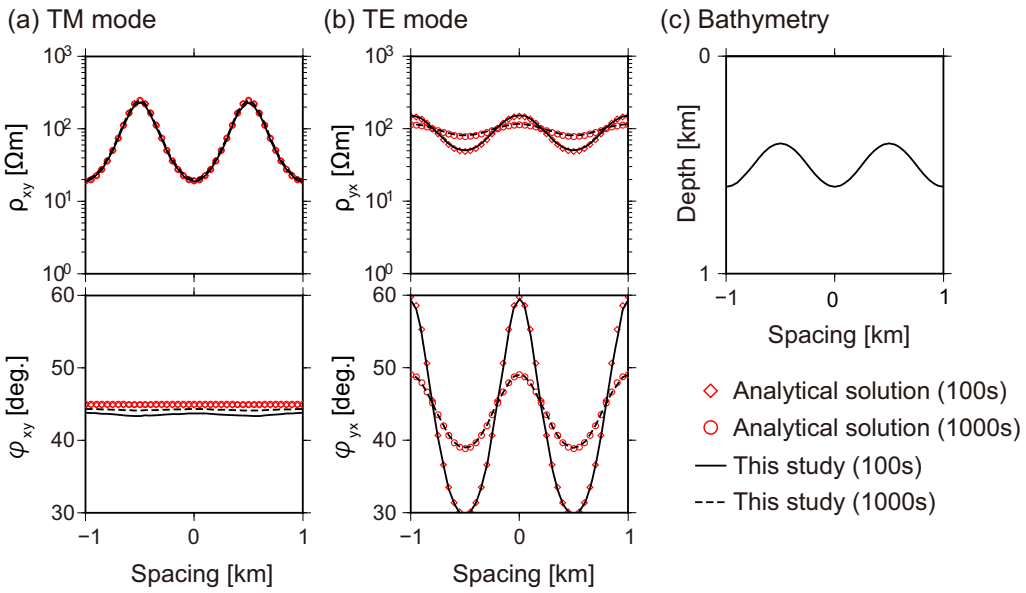

Figure 3. Comparison of the seafloor MT response functions calculated in this study with analytical solutions. (a) TM-mode apparent resistivity and phase. (b) TE-mode apparent resistivity and phase. (c) Seafloor topography. The TM-mode analytical solutions were obtained by the modified TM-mode analytical formulation developed in this work (Appendix A) while the TE-mode analytical solutions were obtained by the analytical formulation proposed by Schwalenberg & Edwards (2004).

in the subseafloor region. Therefore, prior to the evaluation of forward calculation results, we developed a general analytical formulation of the TM-mode for a 2-D sinusoidal topography by modifying the TM-mode analytical formulation proposed by Schwalenberg & Edwards (2004) to take into account the contributions of the vertical electric field to the tangential electric field on the interface. The details of the modification is shown in Appendix A.

Calculated apparent resistivity and phase are compared with analytical solutions in Fig. 3. The TM-mode analytical solutions were obtained by the modified TM-mode analytical formulation illustrated in Appendix A while the TE-mode analytical solutions were obtained by the analytical formulation proposed by Schwalenberg & Edwards (2004). The maximum number of order n used to obtain the analytical solutions was 99 so as to obtain accurate solutions. Calculated apparent resistivity and phase are close to the analytical solutions. About the TM-mode, the differences between the calculated apparent resistivities and respective analytical solutions are less than 2.2 per cent on logarithmic scale, and the differences between the calculated phases and the analytical solutions are less than 1.6°. On the other hand, about the TE-mode, the differences between the calculated apparent resistivities and respective analytical solutions are less than 1.3 per cent on logarithmic scale, and the differences between the calculated phases and the analytical solutions are less than 1.1°. Therefore, from the verifications using the two bathymetry models, it can be said that the unstructured tetrahedral FEM can calculate MT response functions properly at the observation sites on the seafloor with bathymetry.

2.2 Verification of the inversion calculation

Next, to confirm that the inversion scheme using an unstructured tetrahedral mesh recovers the subseafloor resistivity distribution even when observed data are distorted by bathymetry, the inversion scheme was applied to a synthetic data set affected by bathymetry. The test model has an L-shaped land–sea boundary and an undulating seafloor (Fig. 4a). Specifically, sea depths (km) are given by eq. (2) at the area of $x \leq 45$ km and $y \geq -45$ km.

$$z\ (x, y) = \ 3.0 - 0.5\ \times \sin\left(\frac{2\pi}{30}x\right) \sin\left(\frac{2\pi}{30}y\right) - 0.25\ \times \sin\left(\frac{2\pi}{10}x\right) \sin\left(\frac{2\pi}{10}y\right) - 0.1\ \times \sin\left(\frac{2\pi}{3}x\right) \sin\left(\frac{2\pi}{3}y\right) \tag{2}$$

That is, the seafloor topography comprises sinusoidal undulations at wavelengths of 3, 10 and 30 km. The height of the land area is uniformly 0 km. The distance between the area with the undulations and the land–sea boundary is 10 km. The sea becomes shallower smoothly from the seafloor to the land–sea boundary. Of the 49 observation sites included in the model, 13 sites are located on the land side while the other sites are located on the seafloor with the undulations (Fig. 4). The distances between the adjacent sites are 25 km. The respective maximum and minimum sea depths of these sites are 3.75 and 2.25 km. The effects of the bathymetry on the response functions of the sites are shown in Appendix B.

In the model used to produce the synthetic data set, two resistivity anomalies measuring 50 km × 50 km × 30 km are embedded in a background medium of 100 Ωm. The tops of the blocks are located 20 km below the sea surface. The block resistivities are 10 and 1000 Ωm, respectively. In the synthetic inversion, full components of the impedance tensor and the vertical magnetic transfer function (VMTF) for the 16 periods from 31.6 to 10 000 s were used as data. A Gaussian noise was added to the synthetic data. The standard deviation of the noise

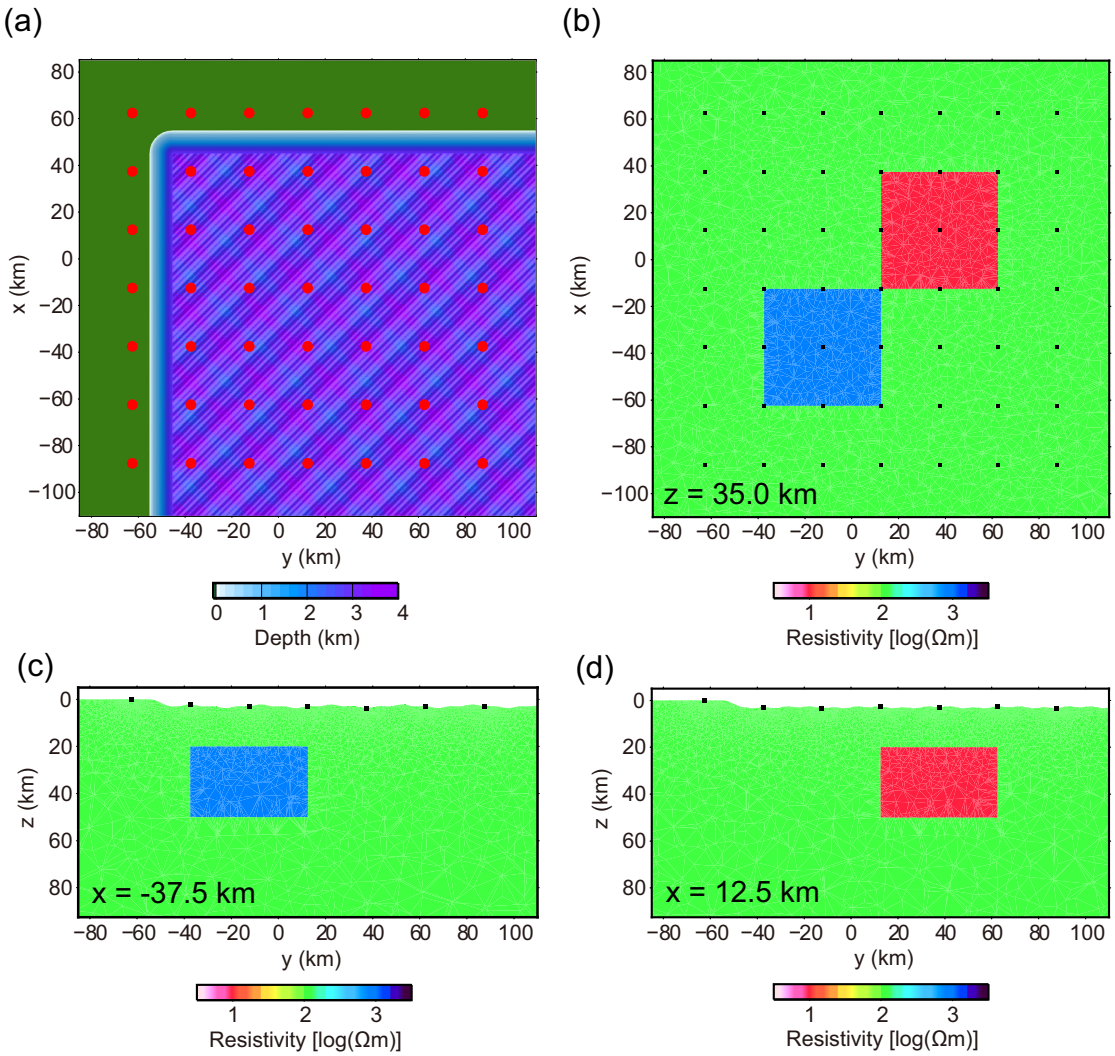

Figure 4. (a) Bathymetry of the model used for the synthetic inversion. (b) Horizontal slice at 35 km depth of the target resistivity structure for the synthetic inversion. (c) and (d) respectively portray vertical slice at $x = -37.5$ km and $x = 12.5$ km. Red dots in (a) and black dots in (b), (c) and (d) denote observation points.

added to the impedance tensor components was 5 per cent of the maximum amplitude of the off-diagonals, that is, $0.05 \times \max(|Z_{xy}|, |Z_{yx}|)$, where Z_{xy} and Z_{yx}, respectively, denote the xy and yx components of the impedance tensor. The standard deviation of the noise added to the VMTF components was 5 per cent of the largest absolute values of $|T_{zx}|$ and $|T_{zy}|$, that is, $0.05 \times \max(|T_{zx}|, |T_{zy}|)$, where T_{zx} and T_{zy}, respectively, represent the x and y components of the VMTF. In addition, when the error of a VMTF component was smaller than 0.05, it was set as 0.05.

The size of the computational mesh used in the synthetic inversion was 3000 km × 3000 km × 3100 km, of which the uppermost 100 km was the air layer. Using TetGen (Si 2007), the model was discretized with 1 343 765 tetrahedral elements. The elements other than those of the air layer or the sea were grouped into 27 732 parameter cells using an algorithm written by Usui (2015). The initial resistivities of the parameter cells were 100 Ωm. The resistivity of the sea was fixed as 0.25 Ωm during the inversion. The trade-off parameter α^2 was set as 31.6. The horizontal EM field at each seafloor site was calculated by the same manner as used in the calculation of the second model of the previous section. On the other hand, at each onshore site, both the horizontal electric field and the horizontal magnetic field were calculated from the electric field of the element just below the site, that is, the element in the subsurface side.

After the fifth iteration of the inversion, the objective function changed less than 1 per cent from the previous values. Consequently, we adopted the model at that iteration as the final model. The RMS of the model was 0.97. The resistivity distribution of the final model is shown left-most in Figs 5(a)–(c). Both the conductive anomaly and resistive anomaly are recovered in the final model. These results confirmed that the inversion using an unstructured tetrahedral mesh enables us to estimate the subseafloor resistivity structure properly in spite of the difficulties related to the bathymetric distortions. In Figs 5(d)–(f), the result of the inversion using a mesh without the land–sea boundary is also shown. In the mesh, the sea depth was assumed to be 3 km outside of the area with the seafloor undulations ($x \leq 45$ km and $y \geq -45$ km) and there was no land area. The number of the mesh elements was 1 292 741. The parameter cells, except for those of the air or the sea,

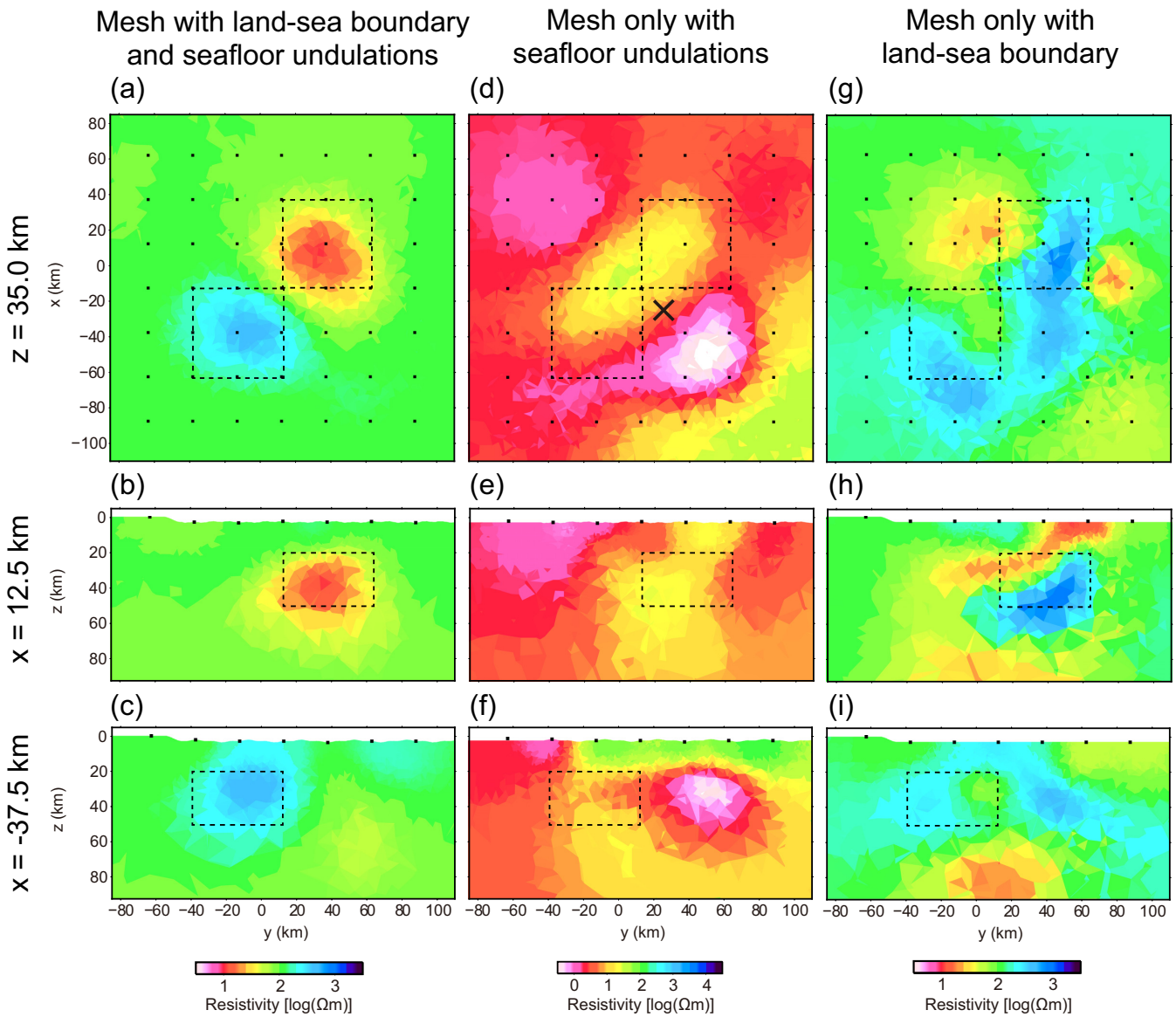

Figure 5. Results of the synthetic inversion tests with meshes of three types. (a–c) Resistivity structure obtained from the mesh into which both the land–sea boundary and the seafloor undulation were incorporated. (d–f) Resistivity structure obtained from the mesh only with the seafloor undulations. (g–i) Resistivity structure obtained from the mesh only with the land–sea boundary. The actual locations of the anomalies are shown with dashed lines. Black dots show observation points. The × mark in (d) shows the centre of the seafloor observation sites.

were 25 247. The other calculation conditions were the same as those described above. After the 13th iteration, the converged solution, with RMS of 6.09, was obtained. When the land–sea boundary was not incorporated into the mesh, the subseafloor resistivity was underestimated. Specifically, the resistivity to the southeast of the centre of the seafloor observation sites, marked in Fig. 5(d), and that around the land–sea boundary were estimated as about 1 Ωm. This underestimation probably occurs because of the lack of the ocean-side coast effect, which lowers the amplitude of the impedance tensor calculated from the mesh without the land–sea boundary. Moreover, we also performed the inversion with the mesh where the undulations of the seafloor were not represented but the land–sea boundary was only incorporated. The mesh consisted of 1 354 427 tetrahedral elements. The elements not belonging to the air and the sea were grouped into 27 769 parameter cells. The other calculation conditions were the same as those used in the previously described calculations. The converged solution, with RMS of 3.29, was obtained after the sixth iteration. When the seafloor undulations were not incorporated into the computational mesh, two anomalies of the original model were not recovered. Instead of them, at the depths less than 20 km, some conductive and resistive anomalies are wrongly estimated. In addition, the resistivity under the centre of the seafloor observation sites is higher than that of the surrounding area. Appendix B shows that the induction arrows at 100 s tend to point towards the direction away from the centre when the seafloor undulations are represented in the mesh. This feature of the induction arrows does not appear without the seafloor undulations. Therefore, it is thought that the inversion ignoring the effects of the undulations wrongly made the resistivity under the centre of the seafloor observation sites higher.

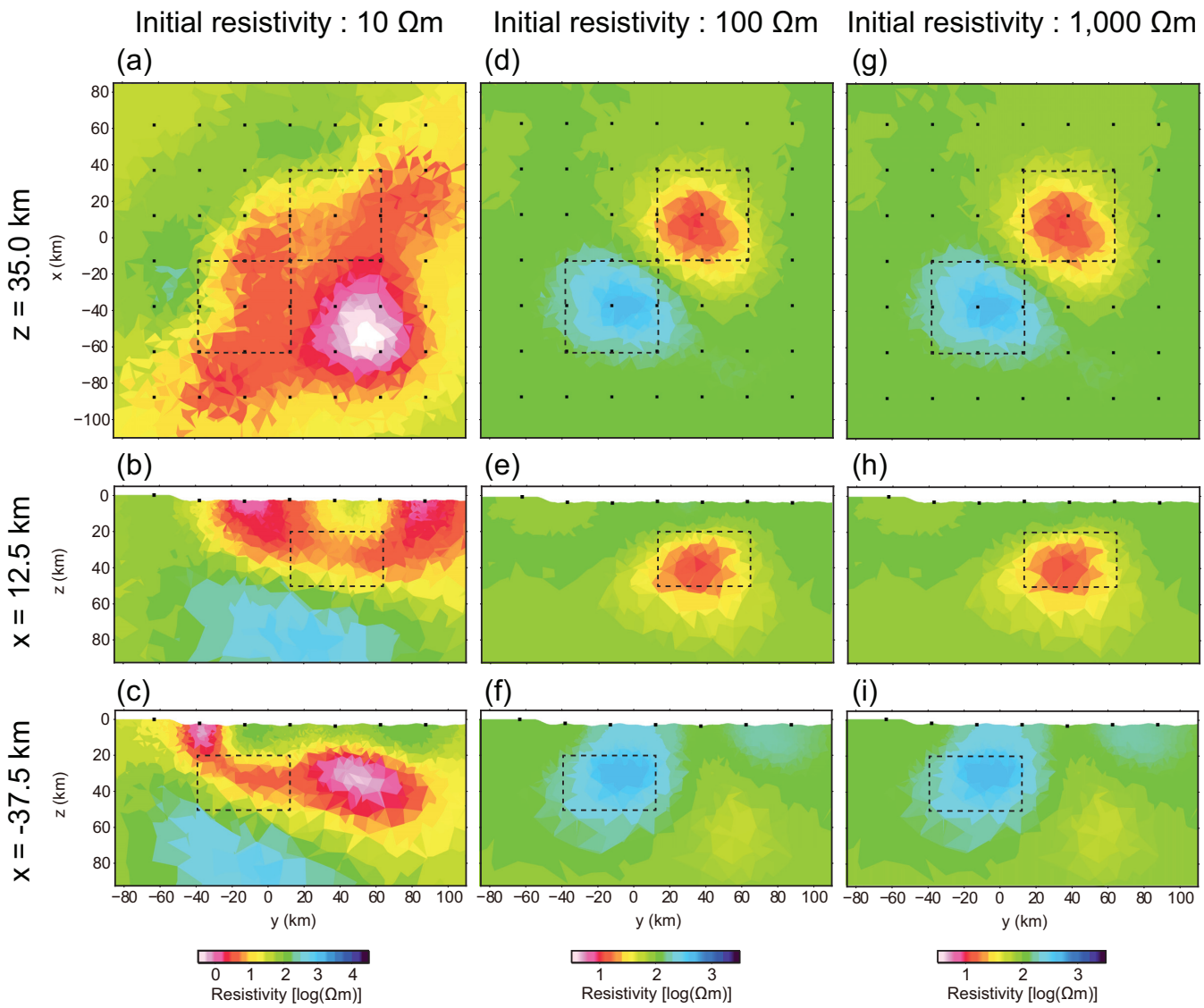

Figure 6. Results of the synthetic inversion tests obtained with different initial models. (a–c) Resistivity structure obtained from the initial model of 10 Ωm. (d–f) Resistivity structure obtained from the initial model of 100 Ωm. (g–i) Resistivity structure obtained from the initial models of 1000 Ωm. The actual locations of the anomalies are shown with dashed lines. Black dots denote observation points.

Furthermore, to assess the dependence of the inversion result on the initial guess of the subsurface resistivity structure, we performed inversions by changing the initial subseafloor resistivity to 10 and 1000 Ωm, respectively. The other calculation conditions were the same as those described previously. As presented in Figs 6(g)–(i), when the initial seafloor resistivity was 1000 Ωm, the obtained resistivity structure was close to that estimated with the initial subsurface resistivity of 100 Ωm. The difference of the RMSs of the two models was less than 0.01. However, when the initial subseafloor resistivity was 10 Ωm, the resistivity to the southeast of the centre of the seafloor observation sites was estimated as about 1 Ωm (Figs 6a–c) as the results obtained with the mesh where the land–sea boundary was not incorporated (Figs 5d–f). The RMS of the result was 5.18, which is more than five times larger than those of the other cases. It is thought that the effect of the land–sea boundary was underestimated in the first few iterations because the initial subseafloor resistivity was underestimated. Consequently, the inversion result got trapped in a local minimum, which is far different from the true model. The dependence on the starting model was also reported in a 2-D marine MT inversion for a model with a land–sea boundary (Worzewski *et al.* 2012).

From the results of the synthetic inversion test, we confirmed that the inversion scheme using an unstructured tetrahedral mesh can give a proper resistivity structure, even for a model with a land–sea boundary and seafloor undulations by incorporating all of them into a computational mesh. However, the synthetic inversion gave a wrong resistivity distribution when we assumed an initial subsurface resistivity lower than the background resistivity of the true resistivity structure. Since inversion results are not independent of the initial model because of the inherent nonlinearity of MT inversion, we should perform inversions with various starting models and then check how much the starting model affects the inversion result.

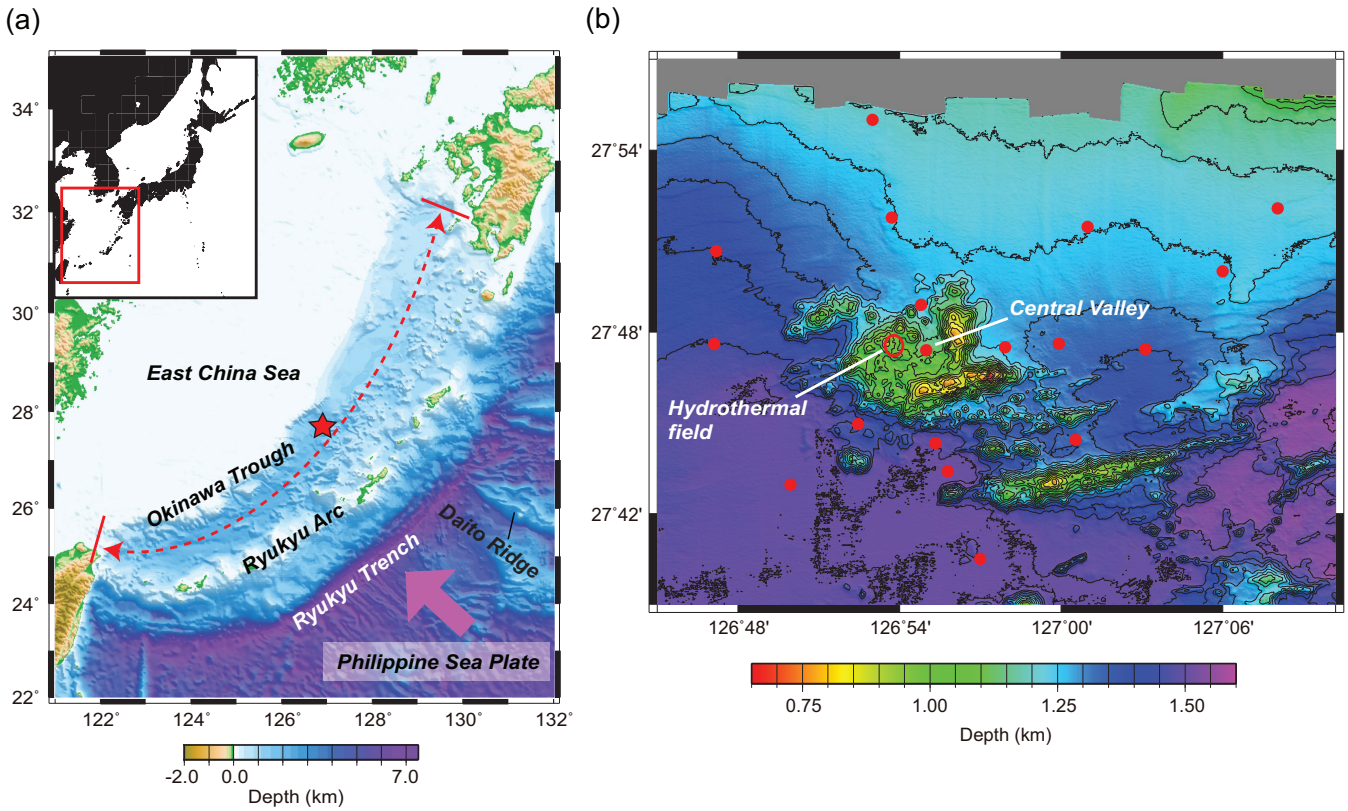

Figure 7. (a) Location map and bathymetry of the Okinawa Trough. The red star represents the Iheya North Knoll location. (b) Bathymetry around the Iheya North Knoll. The high-resolution bathymetry surveyed by JAMSTEC was used to draw the figure. The hydrothermal field of the Iheya North Knoll is shown by a red open circle. Red filled circles represent the seafloor observation sites used for this study.

3 APPLICATION TO ACTUAL MARINE MT DATA OF THE IHEYA NORTH KNOLL

3.1 Iheya North Knoll

We applied the inversion scheme with an unstructured tetrahedral mesh to a marine MT data set observed around the Iheya North Knoll in order to check the scheme's applicability to actual marine MT data. The Iheya North Knoll in the middle Okinawa Trough is located approximately 150 km northwest of Okinawa Island (Fig. 7). The Okinawa Trough, extending from South Kyushu of the Japanese mainland to North Taiwan, is a backarc basin behind the Ryukyu trench-arc system in the East China Sea. It was formed by the subduction of the Philippine Sea Plate beneath the Eurasia Plate at the Ryukyu trench. Based on the results of the past seismic studies, the crustal structure of the Okinawa Trough is considered to be continental rather than oceanic (e.g. Nagumo *et al.* 1986; Sato *et al.* 1994), and is regarded as the only existing marginal backarc basin in the rifting stage (Letouzey & Kimura 1986), although the commencing time and detailed history of the lifting remain controversial (e.g. Miki 1995; Kimura 1996; Sibuet *et al.* 1998). The Moho is located at around 20 km below the sea surface in the middle Okinawa Trough (Nishizawa *et al.* 2011).

The Iheya North Knoll is located at the northwestern end of the Volcanic Arc Migration Phenomenon (VAMP) area (Sibuet *et al.* 1998). This area, which is regarded as the prolongation of the Daito Ridge (Fig. 7; Sibuet *et al.* 1998), is characterized by high heat flow (Yamano *et al.* 1989) and several hydrothermal fields including the Iheya North Knoll (Ishibashi *et al.* 2015). In the Iheya North Knoll, the volcanic body penetrates through a sedimentary sequence and rises about 500 m above the seafloor (Tsuji *et al.* 2012). The eastern flank of the western peak of the knoll (marked in Fig. 7), facing the Central Valley, is a hydrothermal field with about tens of active hydrothermal mounds (Tsuji *et al.* 2012; Ishibashi *et al.* 2015). The maximum temperature of the fluid discharged from the mounds is 311 °C, suggesting the contribution of magma to the hydrothermal system (Tsuji *et al.* 2012). In 2010, Integrated Ocean Drilling Program Expedition 331 conducted drilling in the Central Valley, revealing that the sediments there are mainly pelagic/hemipelagic mud and coarse volcanoclastic deposits (Expedition 331 Scientists 2010). Furthermore, Tsuji *et al.* (2012) conducted a seismic reflection survey around the Iheya North Knoll, which revealed that porous and permeable volcanoclastic sequences are interbedded within pelagic and hemipelagic sediments. They inferred that the hydrothermal system around the knoll has lateral scale greater than several kilometres and that the volcanoclastic sequences and normal faults act as migration pathways of hydrothermal fluid.

Even though the electrical resistivity is a physical property that is useful to elucidate the Earth's interior, resistivity structure of the Okinawa Trough has rarely been estimated. Shimakawa & Honkura (1991) estimated a 2-D resistivity structure along a profile orthogonal to the Ryokyu trench-arc system by using the magnetic transfer function. However, Shimakawa & Honkura (1991) only provided a rough

resistivity structure up to 150 km below ground because the minimum period of the data was 30 min and because the observation sites were sparsely distributed. Furthermore, in the previous study, the resistivities of the conductive layer and the underlying basement layer, as well as the thickness of the conductive layer, were not determined from a modelling but were instead inferred from the results of the older geophysical studies. This study is, thus, the first approach to unveil detail resistivity structure under the Okinawa Trough.

3.2 Observed data

We used the data set obtained by a marine magnetotelluric survey conducted by the Japan Agency for Marine-Earth Science and Technology (JAMSTEC) using OBEMs developed by JAMSTEC (Kasaya & Goto 2009). The number of measurement sites used for this study were 18 (Fig. 7). At all sites, both the electric field and magnetic field were observed. We estimated the impedance tensor and the VMTF from the observed data using a robust magnetotelluric response function estimator (Chave & Thomson 2004). The period range used in the MT modelling was from 32 to 8192 s. The response functions at about seven periods per decade were used, although noisy data were removed by visual inspection.

Fig. 8(a) shows the maps of the swift strike (Swift 1967) and the induction arrow (Parkinson convention) calculated from the observed data. At 64 s, induction arrows seem to point away from the knoll, although swift strikes appear to be directed in various directions. This feature of the induction arrows is probably attributable to the bathymetric effect on the geomagnetic field because induction arrows point to the deeper sea. For longer periods, swift strikes are aligned to about N40°E – S40°W or S50°E – N50°W. Furthermore, at 4.096 s, the real arrows point towards the direction of S50°E. Open circles with error bars in Fig. 9(a) show the observed apparent resistivity and phase in the rotated coordinate frame where the plus-x direction corresponds to N40°E, which is approximately parallel or perpendicular to the swift strikes at 256, 1024 and 4096 s. In the rotated coordinate, the apparent resistivity of the *xy* component increases continuously from about 3 Ωm at 32 s to about 100 Ωm at around 2500 s and then turns to decline, whereas the apparent resistivity of the *yx* component remains almost constant at about 5 Ωm. In Fig. 9, the response functions of the three representative sites are illustrated, however the apparent resistivities at the other sites show similar anisotropy.

3.3 Forward calculation using the mesh with bathymetry

It is possible that the anisotropic off-diagonal components of the rotated impedance tensors are attributed to the bathymetry of the survey area. On the seafloor, the apparent resistivity calculated from the electric field perpendicular to the coast decreases due to the galvanic ocean-side coast effect (Constable *et al.* 2009). Constable *et al.* (2009) reported a similar splitting of the apparent resistivity observed at sites in the San Diego Trough. Although the Iheya North Knoll has no nearby coastline, there is the East China Sea, where the sea depth is several hundred metres at most, to the west of the knoll. Therefore, it can be inferred that the East China Sea functions similarly to the land and that it causes the differences of the off-diagonals.

To test the hypothesis, we performed a forward calculation with a computational mesh by incorporating the bathymetry around the Iheya North Knoll (Fig. 10). The size of the computational domain was 3000 km × 3000 km × 3100 km, including the 100 km air layer at the top. The horizontal centre of the mesh (E126.92°, N27.79°) was located at the Central Valley of the Iheya North Knoll. The positive *x*-axis corresponds to the north. The mesh included the bathymetry around the Iheya North Knoll as well as the topography of the Eurasian continent, Japanese main islands and the islands around the Ryukyu Arc. The edge lengths became shorter when approaching the observation sites. Those were scaled down to approximately 100 m adjacent to the sites, whereas edge lengths were about 150 km at the outermost region. The total number of elements was 1 667 663. The elements except those belonging to the air or the sea were grouped into 24 087 parameter cells.

The mesh was produced using the following three steps (Fig. 11). First, the land–sea boundaries within the computational domain were defined. The coastlines were extracted from the low-resolution data of the Global Self-consistent Hierarchical High-resolution Shorelines Coastline Database (Wessel & Smith 1996), which was thinned out preliminarily to suppress the number of the tetrahedral elements that were finally generated. Second, the surface mesh covering the computational domain was generated. In the surface mesh, the top, bottom and sides of the computational domain were defined as well as the sea surface and the Earth's surface. All of the surfaces consist of triangle elements. Among them, the last two surfaces were inner surfaces, where precise topography and bathymetry were represented. To produce the surfaces, a 2-D triangle mesh was first generated without breaking the land–sea boundaries defined previously, using the Delaunay triangulation method with boundary constraint (Cheng *et al.* 2012). Then heights (*z*-coordinates) of the points of the 2-D mesh were interpolated from the high-resolution bathymetric data with 30-m grid, which was acquired by JAMSTEC, JODC-Expert Grid data for Geography-500 m (J-EGG500) and ETOPO1 (Amante & Eakins 2009). The first data were used in the area around the Iheya North Knoll (E126.73°–E127.33°, N27.20°–N27.92°). The second data were used in the area around Japan (E124.00°–E130.00°, N24.00°–N30.00°), except for the area in which the first data were used. The third data were used for the other area. After merging all of the data sets, we calculated the *z*-coordinate of each node on the land surface or on the seafloor by the inverse distance weighted method. That is to say, we calculated the *z*-coordinate of each node as

$$\frac{\sum_{i=1}^{4}(z_i/r_i)}{\sum_{i=1}^{4}(1/r_i)}, \tag{3}$$

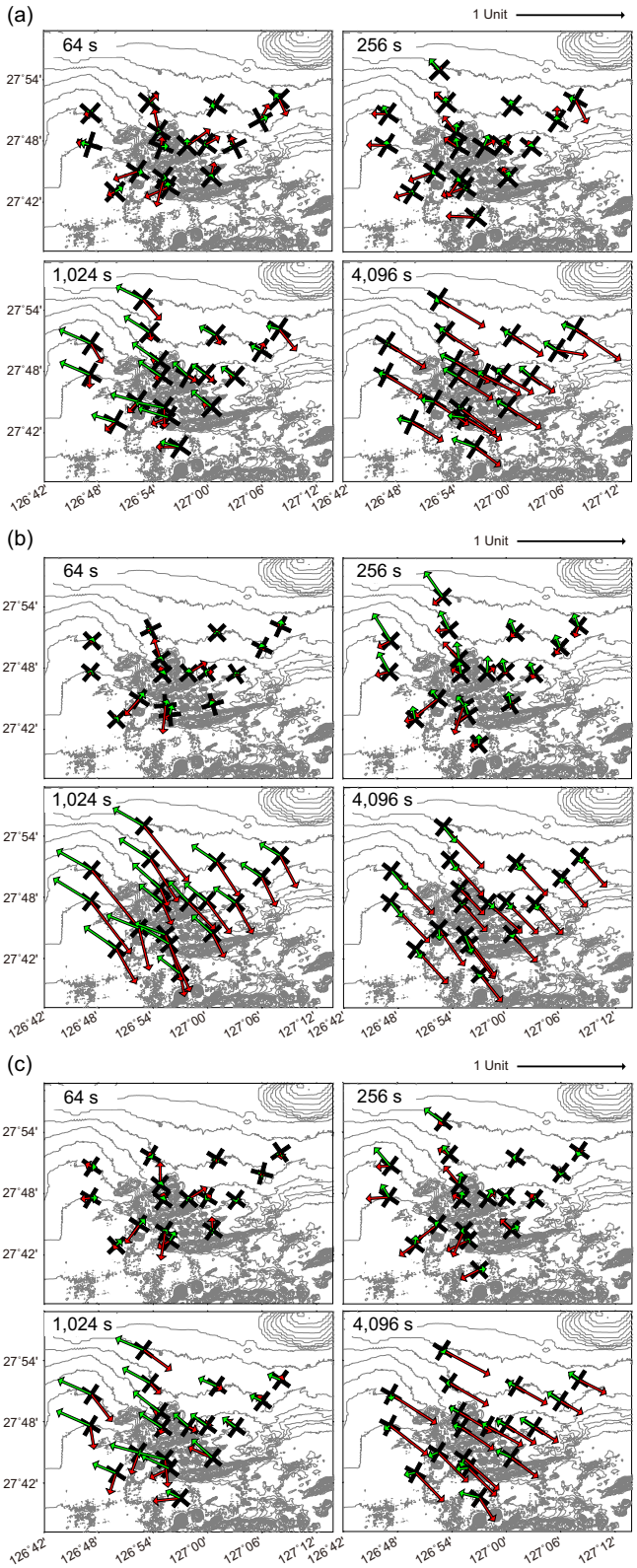

Figure 8. Swift strikes and induction arrows (Parkinson convention) calculated from (a) the observed data, (b) the simple two-layered model with the bathymetry (Fig. 12) and (c) the best model obtained by the inversion analysis. Black lines represent the direction of the swift strikes of the observation sites. Red and green arrows, respectively, indicate real and imaginary vectors.

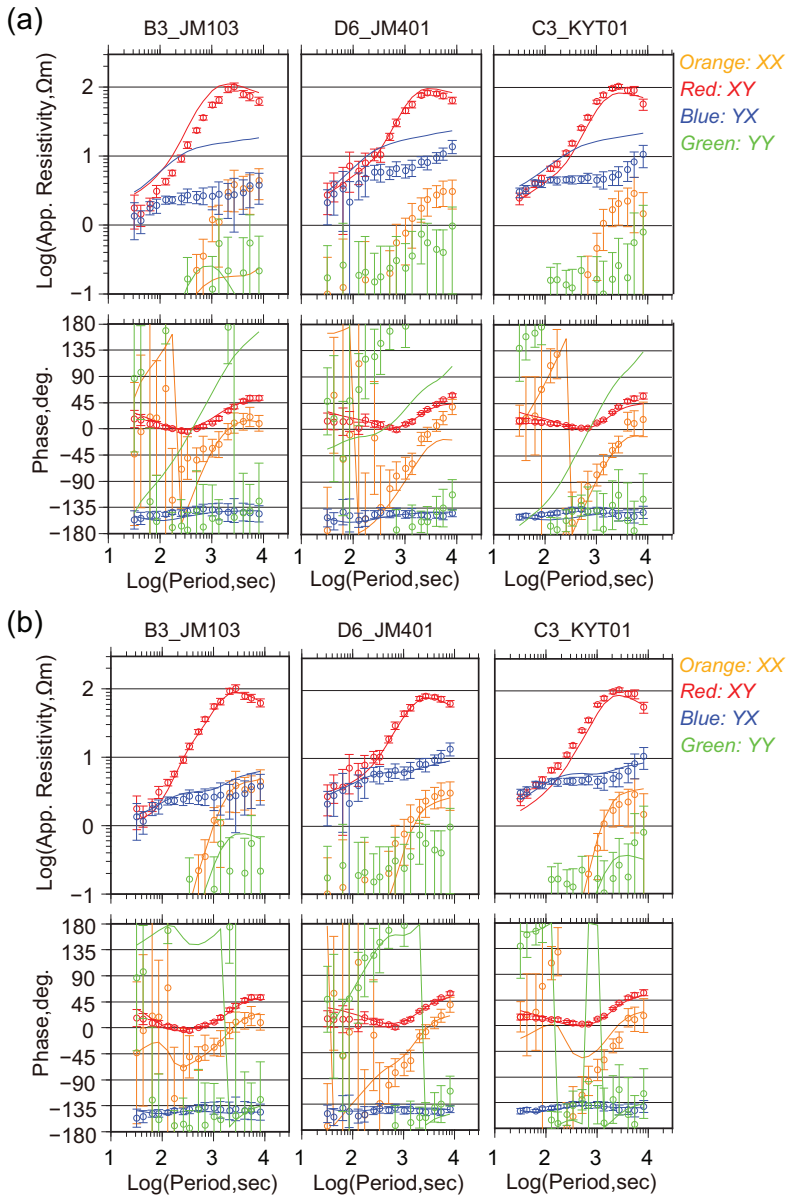

Figure 9. Comparison of the observed apparent resistivity and phase with (a) the forward results obtained from the simple two-layered model with the bathymetry (Fig. 12) and (b) the response functions calculated from the best model of the inversion analysis. These response functions are the ones in the coordinate where the plus-x direction corresponds to N40°E. Open circles with error bars denote the observed data while solid lines represent the calculated response functions. Locations of the representative three sites are shown in Fig. 12(c).

where $z_1, \ldots, z_4$ are the z-coordinates of the four data points nearest to the node and $r_1, \ldots, r_4$ are the horizontal distances between the data points and the node. Finally, 3-D mesh was generated from the surface mesh using TetGen (Si 2007).

As the subseafloor resistivity structure, a simple model consisting of an upper conductive layer and an underlying resistive layer was assumed (Fig. 12). Specifically, a 4-km thick 3 Ωm layer was assumed under the entire seafloor. The resistivity of the underlying layer was assumed to be 100 Ωm homogeneously. The resistivity of the sea was set as 0.25 Ωm. The conductive layer thickness and the resistivity of each layer were determined by trial-and-errors to decrease the RMS misfit of the forward result. The RMS misfit calculated from the forward calculation result was 3.04. The swift strikes and the induction arrows calculated from the result of the forward calculation are shown in Fig. 8(b). The calculated real arrows at 64 s point away from the knoll, as do the observed ones. Therefore, it is confirmed that this feature of the observed data derives from the bathymetric effect due to the uplifted volcanic body of the knoll. At 256, 1024 and 4096 s, the swift strikes from the result of the forward calculation are aligned to the similar direction with those of the observed data (N40°E – S40°W or S50°E – N50°W). In addition, the real arrows at 4096 s point southeast, which is also consistent with the observed ones. However, the calculated real arrows at 1024 s point southeast, whereas the observed ones at the period do not show such a feature. This difference is probably attributable to the difference between the assumed simple resistivity structure and the actual one.

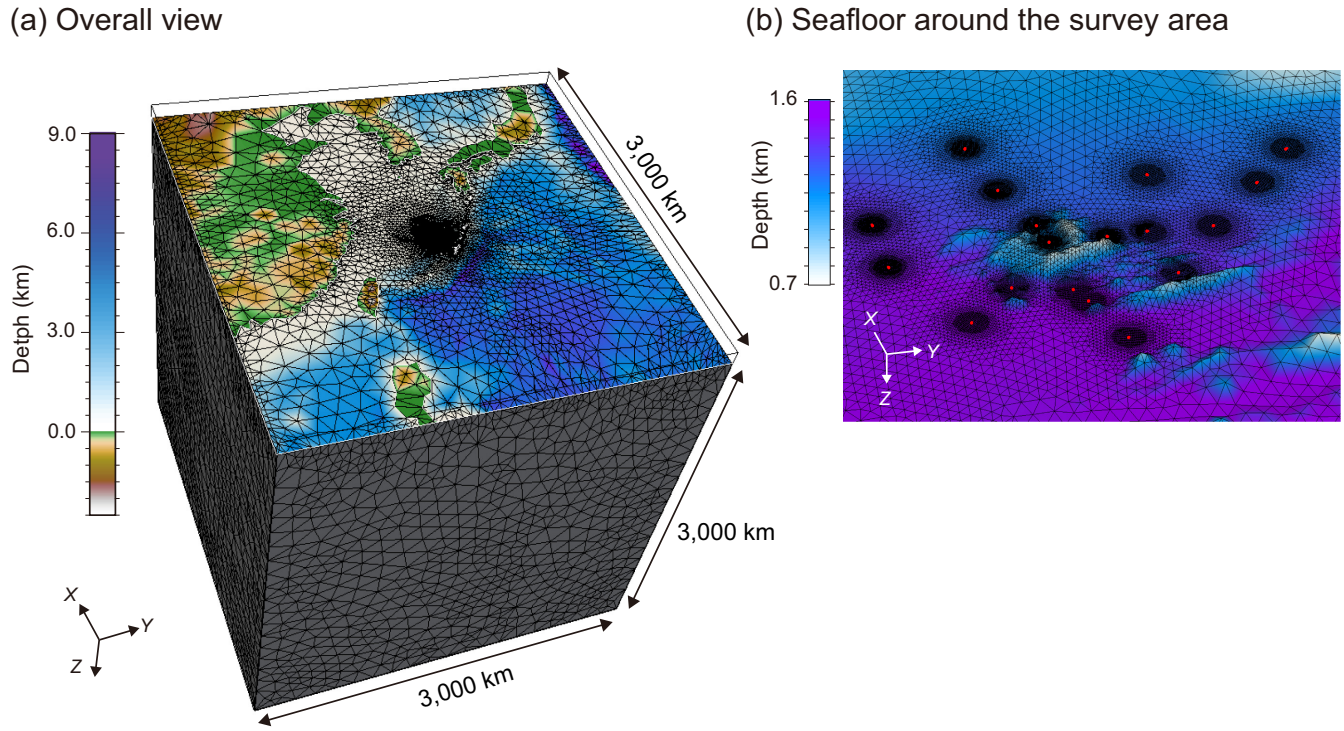

Figure 10. Computational mesh used for the MT modelling of the observed data around the Iheya North Knoll. The horizontal centre of the mesh was located at the Central valley of the Iheya North Knoll. The positive *x*-direction corresponds to the north. (a) Overall view of the mesh. Elements belonging to the air layer or the sea are omitted to improve the visibility of the Earth's surface within the mesh. (b) Surface mesh around the survey area. Height differences are emphasized by enlarging the vertical coordinates two times.

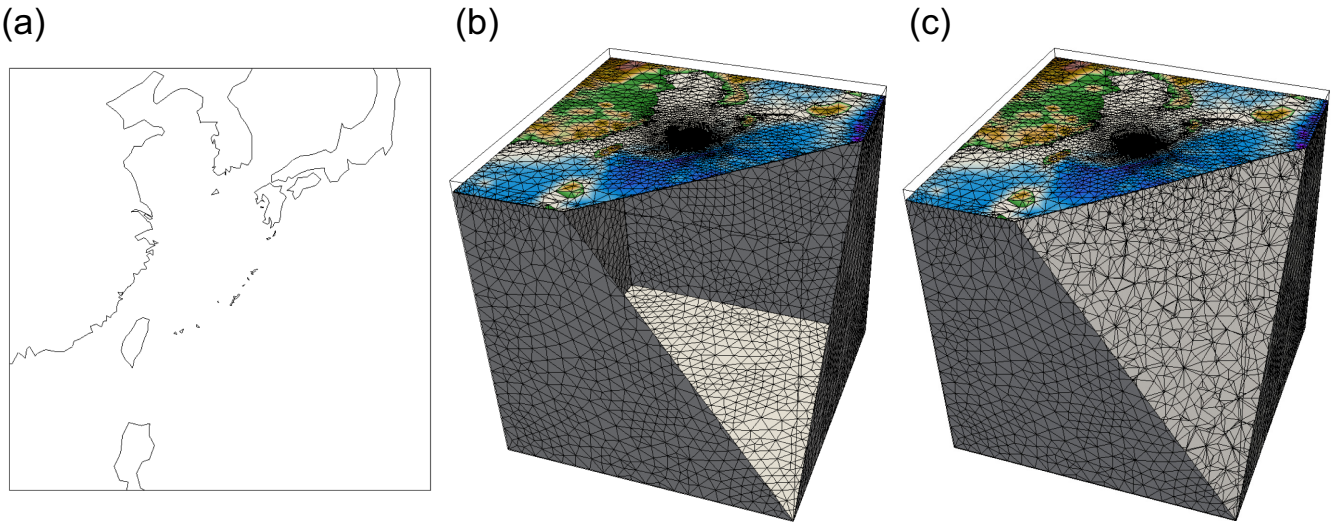

Figure 11. Schematic figure representing the three steps to produce a mesh including the actual bathymetry and topography. (a) First, the land–sea boundaries within the computational domain were defined. (b) Second, the surface mesh covering the computational domain was generated. (c) Finally, 3-D mesh was generated from the surface mesh.

The solid lines in Fig. 9(a) represent the calculated apparent resistivity and phase in the rotated coordinate, showing that the *xy* components of the calculated response functions closely approximate the observed ones and showing that the splitting of the apparent resistivity of the off-diagonals is also reproduced. The splitting is not reproduced when the minimum sea depth is forced to be 1 km in the computational mesh. Specifically, at the second step of the mesh-creating procedure described above (Fig. 11b), when the interpolated sea depth of a node belonging to the seafloor was less than 1 km, the depth of the node was forced to be 1 km. Because the shallow East China Sea is not represented in the mesh with such a modification, it is suggested that the anisotropic off-diagonals are caused by the shallow East China Sea. The fact that the characteristics of the observed response functions were reproduced by the simple two-layer structure and bathymetry demonstrates that the observed data around the Iheya North Knoll depend strongly on the bathymetry around the area, especially on the

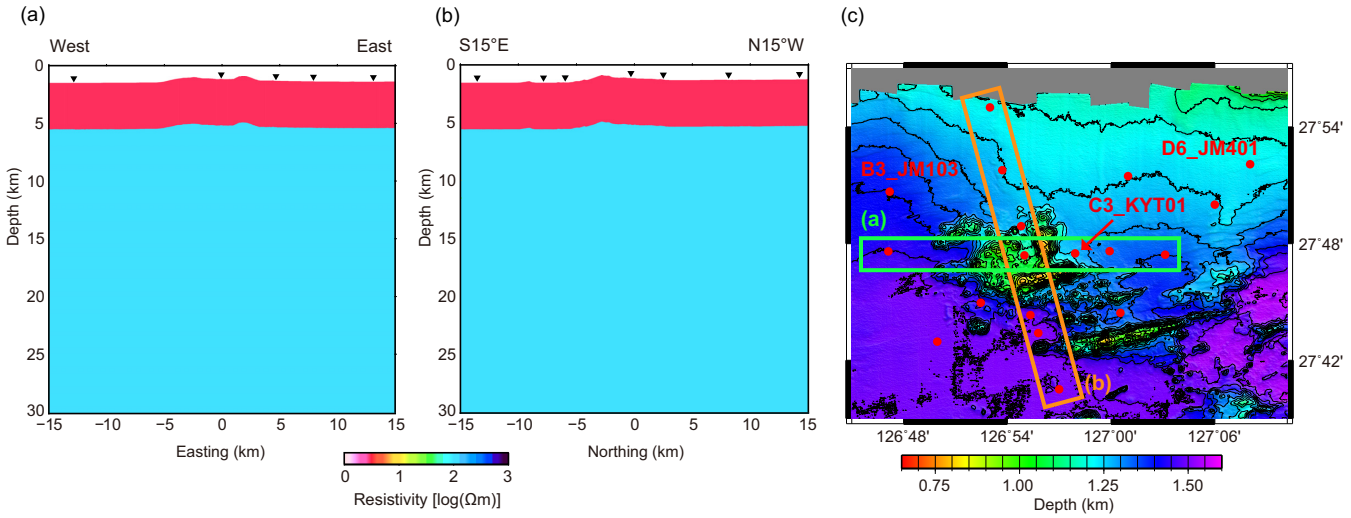

Figure 12. Vertical cross-sections of the two-layered model used to evaluate the bathymetric effect to the observed response functions around the Iheya North Knoll. (a) Cross-section along the profile directed to N15°W–S15°E. (b) Cross-section along the E–W profile. Inverted triangles in (b) and (c) show the locations of the observation sites within ±2.5 km of the profiles. (c) Locations of the profiles of (a) and (b).

sea-depth differences between the depression of the trough and the shallow East China Sea. These results underscore the need to consider the effects of the bathymetry during the interpretation of the observed MT data around the Iheya North Knoll.

3.4 Calculation condition of inversion

We then applied the inversion scheme of Usui (2015) to the observed data. The computational mesh used for the inversion was identical to that used in the forward calculation described above, and therefore the input response functions were the ones in the coordinate with the positive x-direction corresponding to the north. The error floor of each impedance tensor component was 5 per cent of the largest absolute value of the off-diagonals, that is, $0.05 \times \max(|Z_{xy}|, |Z_{yx}|)$. The error floor of each VMTF component was 5 per cent of the largest absolute value of its components, that is, $0.05 \times \max(|T_{zx}|, |T_{zy}|)$. In addition, when the error of a VMTF component was less than 0.05, it was set as 0.05.

The elements except for those belonging to the air layer or the sea were grouped into 24 087 parameter cells. The initial model was the two-layer structure used for the forward calculation described above. The resistivity of the sea was fixed at 0.25 Ωm during the inversion. In the inversion, galvanic distortion was not considered because the galvanic effects from near-seafloor anomalies are considered to be small (Constable *et al.* 2009). As in the previous works (e.g. Patro *et al.* 2005; Matsuno *et al.* 2014), trade-off parameter α^2 was selected by the L-curve criteria from the results obtained by seven different α^2's: 0.0316, 0.100, 0.316, 1.00, 3.16, 10.0 and 31.6. The obtained L-curve and the optimum trade-off parameter are presented in the next section.

3.5 Results and discussion

For all seven trade-off parameters α^2, we obtained converged solutions. Fig. 13 shows the L-curve drawn from the data misfit and the model roughness of these results, demonstrating that the point corresponding to the model of $\alpha^2 = 1.0$ appears to be the 'knee' of the curve, that is, the most preferable model. Therefore, we selected the model of $\alpha^2 = 1.0$, of which the RMS was 1.23, as the best model. In Fig. 8(c), the swift strikes and the induction arrows calculated from the best model are shown. Moreover, the sounding curves calculated from the best model are compared with the observed ones in Fig. 9(b). These figures illustrate that the response functions calculated from the resistivity structure estimated by the inversion are closer to the observed ones than the forward modelling results described in Section 3.3.

Fig. 14 presents the vertical cross-sections of the N15°W–S15°E and E–W profiles through the centre of the model, which is located at the Central Valley of the Iheya North Knoll. In addition, horizontal section views are presented in Fig. 15. The obtained resistivity structure is characterized by a conductive surface layer and the underlying resistive layer, similar to the initial resistivity structure. It is noteworthy that a similar resistivity structure was obtained when the initial subsurface resistivity was homogeneously 10 or 100 Ωm, meaning that the obtained resistivity structure is nearly independent of the initial resistivity structure. The resistivity of the conductive layer is less than 3 Ωm immediately below the seafloor. The conductive layer is consistent with the interpretation of Tsuji *et al.* (2012) that volcanoclastic sequences in sediment layers act as the migration paths of the hydrothermal fluid flow, because the salinity pore water in marine sediment can significantly reduce the resistivity of the sediment (Constable *et al.* 2009). However, at around 5 km depth below the knoll (shown by white dotted lines in Fig.14), the resistivity of the conductive layer is about 10 Ωm, which is slightly higher than that of the surrounding area (approx. 3 Ωm). In order to check the sensitivity to the lateral difference of the resistivity, a constrained inversion was carried out. Specifically, we performed the inversion by forcing the resistivity at depths shallower than 5 km below the sea surface around the survey area to be greater than or equal

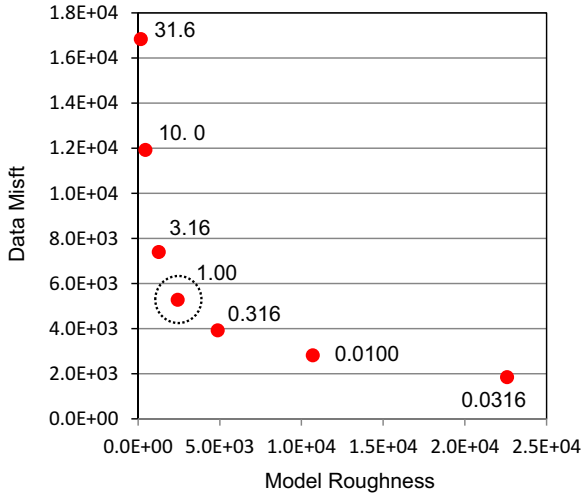

Figure 13. L-curve obtained from the results of the 3-D inversion with various trade-off parameters α^2. The horizontal and vertical axes, respectively, present the model roughness term and data misfit term of the objective function. Numbers adjacent to the points represent the values of parameter α^2, giving the corresponding result. The point surrounded by a dotted circle corresponds to the best model selected in this study ($\alpha^2 = 1.00$).

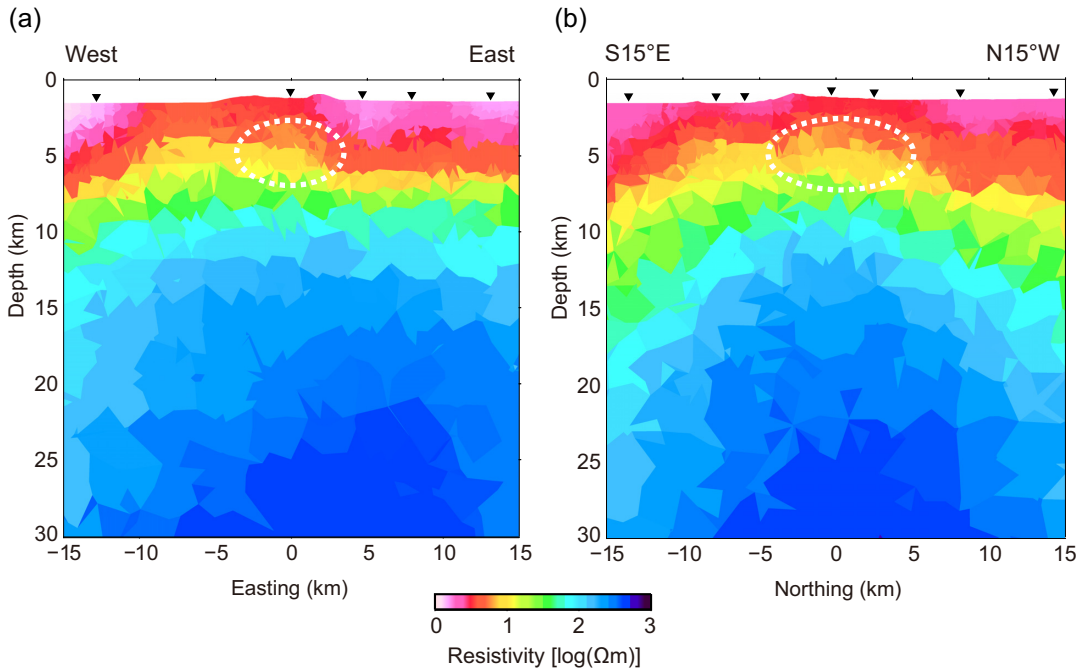

Figure 14. Vertical cross-sections of the 3-D resistivity structure around the Iheya North Knoll. (a) Cross-section of the profile along the E–W direction. (b) Cross-section along the N15°W–S15°E profile. Locations of the profiles are shown in Fig. 12(c). Inverted triangles represent the locations of the observation sites within ±2.5 km of the profiles. The area surrounded by white dotted lines, which is located below the Iheya North Knoll, has slightly higher resistivity (approx. 10 Ωm) than that of the surrounding area.

to 3 Ωm. The RMS of the result of the constrained inversion is 1.37. As in Tada *et al.* (2014), we judged if the difference of the RMS's is significant by a one-sided F test. Because the degrees of freedom, that is the number of data parameters, was 3468, the test statistic is 1.24. The test statistic is greater than the critical value of the 5 per cent significance level (1.06), proving that the increase of the RMS for the constrained inversion model from that for the best model is significant. Therefore, it can be said that the lateral difference of the resistivity of the conductive layer is necessary to explain the observed data. It is known that, just below the knoll, there is a volcanic intrusion that formed the knoll (Tsuji *et al.* 2012). This resistive part in the conductive layer is, therefore, considered to correspond to the consolidated magma intrusion with low porosity, which supplies heat to the hydrothermal system of the knoll.

Moreover, under the conductive layer, the resistivity is about 300 Ωm up to 30 km depth below the sea surface, implying a low content or a low connectivity of conductive materials in the lower crust and the uppermost mantle under the Iheya North Knoll. Additionally, as seen in Fig. 15(a), it is notable that a resistive area (approx. 100 Ωm) extends southeastward from the knoll at 10 km depth. As described in Section 3.3, the real arrows at 1024 s calculated from the simple two-layered medium point southeastward, whereas the observed ones as well as the

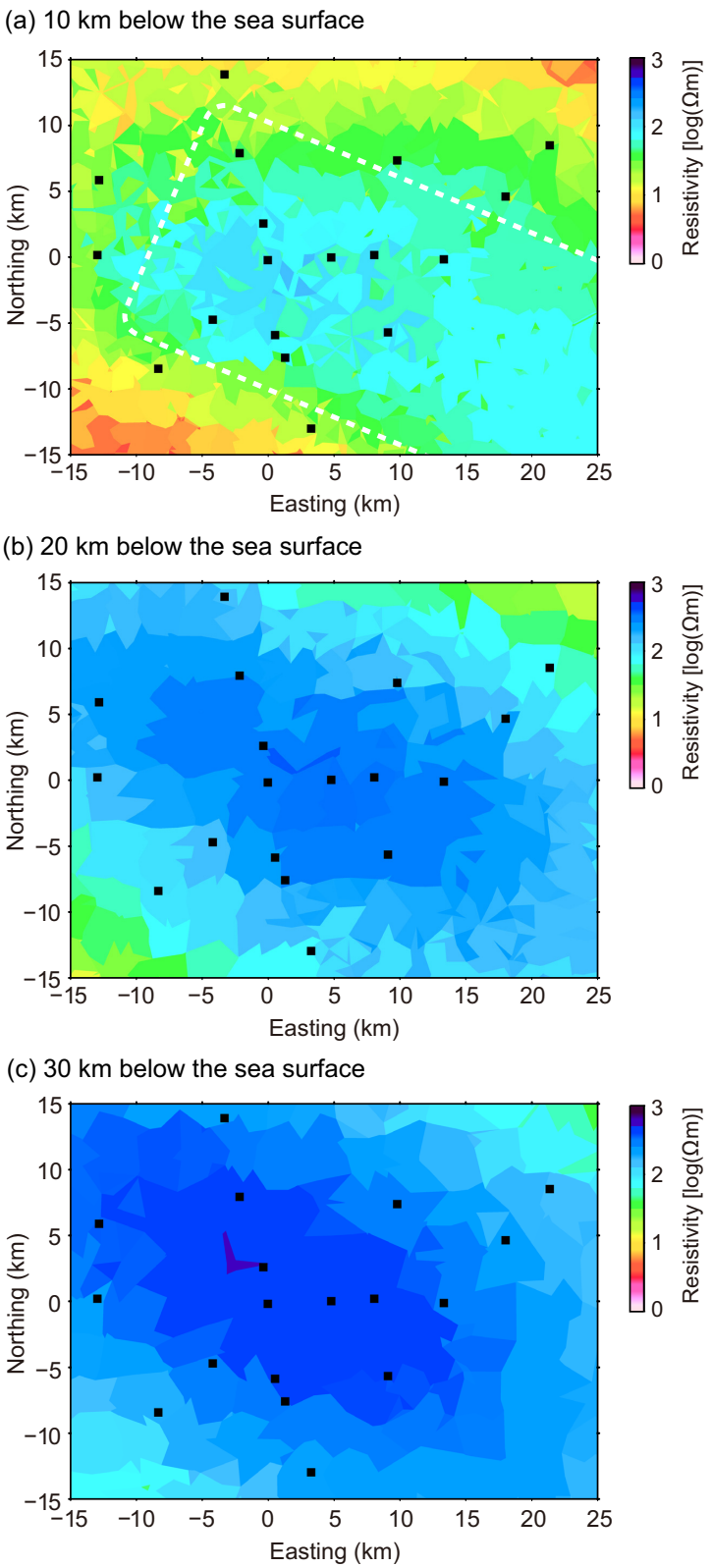

Figure 15. Horizontal cross-sections of the 3-D resistivity structure around the Iheya North Knoll at (a) 10 km, (b) 20 km and (c) 30 km below the sea surface. Black dots denote the observation site locations. The white dotted line in (a) indicates the high resistivity area extending southeastward from the Iheya North Knoll.

inversion results do not (Fig. 8). It is, therefore, considered that the southeast area must be more resistive than the northwest area to cancel out the bathymetric effect that forces the real arrows to point southeastward. To the southeast of the Iheya North Knoll, there are the Yoron Hole Hydrothermal field, the Hakurei Hydrothermal Field and the Clam Hydrothermal field along the Iheya Ridge, which together with the Iheya North Knoll constitute the VAMP area (Ishibashi *et al.* 2015). The VAMP area is characterized by extensive volcanism and anomalous high heat flow (Ishibashi *et al.* 2015). Therefore, the high resistivity of the southeastern side of the Iheya North Knoll implies the existence of consolidated magma under the VAMP area.

4 CONCLUSIONS

We applied an MT inversion scheme using an unstructured tetrahedral mesh (Usui 2015) to the 3-D marine MT problem to confirm its applicability for interpreting the data affected by bathymetry. First, the forward part of the scheme was verified using two models with bathymetry. That verification revealed that the calculated response functions were close to the reference solutions, proving that the 3-D inversion scheme can calculate response functions of the marine MT method accurately. Next, the inversion scheme was applied to a synthetic data affected by a land–sea boundary and seafloor undulations. The true resistivity structure was recovered properly when the bathymetry was incorporated into a computational mesh. Therefore, we confirmed that 3-D inversion using an unstructured tetrahedral mesh enables us to estimate resistivity structure properly from marine MT data affected by bathymetry.

Next, we applied the inversion scheme to the seafloor MT data observed around the Iheya North Knoll of the middle Okinawa Trough. The result of the 3-D modelling using an unstructured tetrahedral mesh with precise bathymetry around the knoll showed that the anisotropic off-diagonals of the rotated impedance tensor and the trends of the induction arrows can be generally explained by the bathymetry. The estimated resistivity structure under the knoll is characterized by a conductive surface layer ($<$10 Ωm) underlain by a resistive layer (approx. 300 Ωm). The conductive layer is consistent with the pelagic/hemipelagic sediments and the highly permeable zones, in which a hydrothermal fluid system was inferred (Tsuji *et al.* 2012). Among the areas, the resistive part immediately below the knoll is considered to correspond to the volcanic intrusion that formed the knoll. No conductive anomaly was detected in the underlying resistive area, implying a low content or a low connectivity of conductive materials in the lower crust and the uppermost mantle under the Iheya North Knoll. Moreover, at around 10 km depth in the resistive area, a resistive area (approx. 100 Ωm) extends southeastward from the Iheya North Knoll, which may imply the consolidated magma under the VAMP area.

In recent years, marine MT surveys are conducted in the areas where 3-D bathymetry strongly influences observed data, such as deep ocean basin and continental margin (e.g. Constable *et al.* 2009; Key & Constable 2011). In the marine MT method, we must incorporate consideration of the bathymetry near the observation sites as well as the regional scale bathymetry far from the sites such as a land–sea boundary for accurate modelling. This study shows that MT inversion with an unstructured tetrahedral mesh can give resistivity structure properly even from marine MT data affected by bathymetry, by accommodating it in a computational mesh. Because it takes into account the bathymetric effects by simply incorporating them into a mesh, this scheme is robustly applicable to various marine MT surveys and thus will help us to estimate subseafloor structures reliably in various areas.

ACKNOWLEDGEMENTS

We are grateful to the members of the Volcanic Fluid Research Center of the Tokyo Institute of Technology for their many helpful suggestions. In addition, we would like to thank two anonymous reviewers and the editor in charge (U. Weckmann) for their valuable comments that significantly improved the manuscript. For this study, we used the computer systems of the Earthquake and Volcano Information Center of the Earthquake Research Institute, The University of Tokyo. Marine MT data acquisition of this study was supported by the Cross-ministerial Strategic Innovation Promotion Program 'Next-generation technology for ocean resources exploration' launched by the Council for Science, Technology and Innovation (CSTI) and managed by the Japan Agency for Marine-Earth Science and Technology (JAMSTEC). Some figures were produced using Generic Mapping Tools (GMT) software (Wessel *et al.* 2013).

REFERENCES

Amante, C. & Eakins, B.W., 2009. ETOPO1 1 arc-minute global relief model: procedures, data sources and analysis, *NOAA Technical Memorandum NESDIS NGDC-24,* pp. 19, Available at:http://www.ngdc.noaa.gov/mgg/global/global.html (accessed 31 May 2015).

Baba, K. & Chave, A.D., 2005. Correction of seafloor magnetotelluric data for topographic effects during inversion, *J. geophys. Res.,* **110**(B12), B12105, doi:10.1029/2004JB003463

Baba, K., Chen, J., Sommer, M., Utada, H., Geissler, W.H., Jokat, W. & Jegen, M., 2016. Marine magnetotellurics imaged no distinct plume beneath the Tristan da Cunha hotspot in the southern Atlantic Ocean, *Tectonophysics,* **716,** 52–63.

Baba, K. & Seama, N., 2002. A new technique for the incorporation of seafloor topography in electromagnetic modelling, *Geophys. J. Int.,* **150**(2), 392–402.

Baba, K., Tada, N., Utada, H. & Siripunvaraporn, W., 2013. Practical incorporation of local and regional topography in three-dimensional inversion of deep ocean magnetotelluric data, *Geophys. J. Int.,* **194**(1), 348–361.

Chave, A.D. & Thomson, D.J., 2004. Bounded influence magnetotelluric response function estimation, *Geophys. J. Int.,* **157**(3), 988–1006.

Cheng, S.-W., Dey, T.K. & Shewchuk, J.R., 2012. *Delaunay Mesh Generation,* CRC Press.

Constable, S., Key, K. , & Lewis, L., 2009. Mapping offshore sedimentary structure using electromagnetic methods and terrain effects in marine magnetotelluric data, *Geophys. J. Int,* **176**(2), 431–442.

Expedition 331 Scientists, 2010, *Deep Hot Biosphere,* IODP Prel. Rept., 331, doi:10.2204/iodp.pr.331.2010.

Fischer, G., 1979. Electromagnetic induction effects at an ocean coast, *Proc. IEEE,* **67**(7), 1050–1060.

Günther, T., Rücker, C. & Spitzer, K., 2006. Three-dimensional modelling and inversion of DC resistivity data incorporating topography—II. Inversion, *Geophys. J. Int.,* **166**(2), 506–517.

Ishibashi, J., Ikegami, F., Tsuji, T. & Urabe, T., 2015. Hydrothermal activity in the Okinawa trough back-arc basin: geological background and hydrothermal mineralization, in *Subseafloor Biosphere Linked to Hydrothermal Systems,* pp. 337–359, eds Ishibashi, J., Okino, K. & Sunamura, M., Springer.

J-EGG500, JODC-Expert Grid data for Geography-500 m. Available at:http://www.jodc.go.jp/data_set/jodc/jegg_intro_j.html (accessed 29 December 2013).

Kasaya, T. & Goto, T., 2009. A small ocean bottom electromagnetometer and ocean bottom electrometer system with an arm-folding mechanism (Technical Report), *Explor. Geophys.,* **40**(1), 41–48.

Key, K., 2012. Marine electromagnetic studies of seafloor resources and tectonics, *Surv. Geophys.,* **33**(1), 135–167.

Key, K., 2016. MARE2DEM: a 2-D inversion code for controlled-source electromagnetic and magnetotelluric data, *Geophys. J. Int.,* **207**(1), 571–588.

Key, K. & Constable, S., 2011. Coast effect distortion of marine magnetotelluric data: insights from a pilot study offshore northeastern Japan, *Phys. Earth planet. Inter.,* **184**(3–4), 194–207.

Key, K. & Weiss, C., 2006. Adaptive finite-element modeling using unstructured grids: the 2D magnetotelluric example, *Geophysics,* **71**(6), G291–G299.

Kimura, M., 1996. Active Rift System in the Okinawa Trough and Its Northeastern Continuation, *Bull. Disas. Prev. Res. Inst., Kyoto Univ.,* **45**(2–3), 27–38.

Letouzey, J. & Kimura, M., 1986. The Okinawa trough: genesis of a back-arc basin developing along a continental margin, *Tectonophysics,* **125**(1–3), 209–230.

Li, S., Booker, J.R. & Aprea, C., 2008. Inversion of magnetotelluric data in the presence of strong bathymetry/topography, *Geophys. Prospect.,* **56**(2), 259–268.

Li, Y. & Key, K., 2007. 2D marine controlled-source electromagnetic modeling: Part 1 — an adaptive finite-element algorithm, *Geophysics,* **72**(2), WA51–WA62.

Matsuno, T., Chave, A.D., Jones, A.G., Muller, M.R. & Evans, R.L., 2014. Robust magnetotelluric inversion, *Geophys. J. Int.,* **196**(3), 1365–1374.

Matsuno, T., Seama, N. & Baba, K., 2007. A study on correction equations for the effect of seafloor topography on ocean bottom magnetotelluric data, *Earth Planet. Sci.,* **59**(8), 981–986.

Miki, M., 1995. Two-phase opening model for the Okinawa trough inferred from paleomagnetic study of the Ryukyu arc, *J. geophys. Res.,* **100**(B5), 8169–8184.

Nagumo, S., Kinoshita, H., Kasahara, J., Ouchi, T., Tokuyama, H., Asamuma, T., Koresawa, S. & Akiyoshi, H., 1986. Report on DELP 1984 cruises in the middle Okinawa trough part 2: seismic structural studies, *Bull. Earthq. Res. Inst. Univ. Tokyo,* **61,** 167–202.

Nishizawa, A., Kaneda, K., Oikawa, M. & Horiuchi, D., 2011. Seismological structure of back arc ocean basin - island arc - trench system in the north of the Nansei Islands, in *Presentation Meeting of Research Products of Hydrographic and Oceanographic Department, Japan Coast Guard* (in Japanese).

Nolasco, R., Tarits, P., Filloux, J.H. & Chave, A.D., 1998. Magnetotelluric imaging of the Society Islands hotspot, *J. geophys. Res.,* **103**(B12), 30 287–30 309.

Patro, B.P.K., Brasse, H., Sarma, S.V.S. & Harinarayana, T., 2005. Electrical structure of the crust below the Deccan Flood Basalts (India), inferred from magnetotelluric soundings, *Geophys. J. Int.,* **163**(3), 931–943.

Sato, T., Koresawa, S., Shiozu, Y., Kusano, F., Uechi, S., Nagaoka, O. & Kasahara, J., 1994. Microseismicity of back-arc rifting in the middle Okinawa Trough, *Geophys. Res. Lett.,* **21**(1), 13–16.

Schwalenberg, K. & Edwards, R.N., 2004. The effect of seafloor topography on magnetotelluric fields: an analytical formulation confirmed with numerical results, *Geophys. J. Int.,* **159**(2), 607–621.

Schwarzbach, C. & Haber, E., 2013. Finite element based inversion for time-harmonic electromagnetic problems, *Geophys. J. Int.,* **193**(2), 615–634.

Shimakawa, Y. & Honkura, Y., 1991. Electrical conductivity structure beneath the Ryukyu trench-arc system and its relation to the subduction of the Philippine sea plate, *J. Geomagn. Geoelectr.,* **43**(1), 1–20.

Sibuet, J.C., Deffontaines, B., Hsu, S.K., Thareau, N., Le Formal, J.P. & Liu, C.S., 1998. Okinawa trough backarc basin: Early tectonic and magmatic evolution, *J. geophys. Res.,* **103**(B12), 30245–30267.

Si, H., 2007. TetGen: a quality tetrahedral mesh generator and 3D Delaunay triangulator, Available at: http://tetgen.berlios.de (accessed 22 February 2014).

Swift, C.M.J., 1967. A magnetotelluric investigation of an electrical conductivity anomaly in the southwestern United States, in *Magnetotelluric Methods,* pp. 156–166, ed. Vozoff, K., Soc. Expl. Geophys.

Tada, N., Baba, K., Siripunvaraporn, W., Uyeshima, M. & Utada, H., 2012. Approximate treatment of seafloor topographic effects in three-dimensional marine magnetotelluric inversion, *Earth Planet. Sci.,* **64**(11), 1005–1021.

Tada, N., Baba, K. & Utada, H., 2014. Three-dimensional inversion of seafloor magnetotelluric data collected in the Philippine sea and the western margin of the northwest Pacific Ocean, *Geochem. Geophys. Geosyst.,* **15**(7), 2895–2917.

Tada, N., Tarits, P., Baba, K., Utada, H., Kasaya, T. & Suetsugu, D., 2016. Electromagnetic evidence for volatile-rich upwelling beneath the Society hotspot, French Polynesia, *Geophys. Res. Lett.,* **43**(23), 12021–12026.

Tsuji, T. *et al.*, 2012. Hydrothermal fluid flow system around the Iheya North Knoll in the mid-Okinawa trough based on seismic reflection data, *J. Volcanol. Geotherm. Res.,* **213–214,** 41–50.

Usui, Y., 2015. 3-D inversion of magnetotelluric data using unstructured tetrahedral elements: applicability to data affected by topography, *Geophys. J. Int.,* **202**(2), 828–849.

Usui, Y., Ogawa, Y., Aizawa, K., Kanda, W., Hashimoto, T., Koyama, T., Yamaya, Y. & Kagiyama, T., 2017. Three-dimensional resistivity structure of Asama Volcano revealed by data-space magnetotelluric inversion using unstructured tetrahedral elements, *Geophys. J. Int.,* **208**(3), 1359–1372.

Utada, H., 2015. Review electromagnetic exploration of the oceanic mantle, *Proc. Japan Acad. B,* **91**(6), 203–222.

Wessel, P. & Smith, W.H.F., 1996. A global self-consistent, hierarchical, high-resolution shoreline database, *J. geophys. Res.,* **101**(B4), 8741–8743.

Wessel, P., Smith, W.H.F., Scharroo, R., Luis, J. & Wobbe, F., 2013. Generic mapping tools: improved version released, *EOS, Trans. Am. geophys. Un.,* **94**(45), 409–410.

Worzewski, T., Jegen, M. & Swidinsky, A., 2012. Approximations for the 2-D coast effect on marine magnetotelluric data, *Geophys. J. Int.,* **189**(1), 357–368.

Yamano, M., Uyeda, S., Foucher, J.P. & Sibuet, J.C., 1989. Heat flow anomaly in the middle Okinawa Trough, *Tectonophysics,* **159**(3–4), 307–318.

APPENDIX A: A GENERAL TM-MODE ANALYTICAL FORMULATION FOR A 2-D SINUSOIDAL TOPOGRAPHY

In the TM-mode analytical formulation proposed by Schwalenberg & Edwards (2004), contributions of the vertical electric field to the tangential electric field on the interface between the upper region and the lower region are neglected, and it is assumed that the horizontal

$$
\begin{pmatrix}
0 & 0 & 0 & 0 & 0 & 0 \\
0 & 0 & \frac{1}{2}\frac{\nu^2\Delta}{\mu_0\sigma_1}I_0(\theta_1^1\Delta)-\frac{1}{2}\frac{\nu^2\Delta}{\mu_0\sigma_1}I_2(\theta_1^1\Delta) & -\frac{1}{2}\frac{\nu^2\Delta}{\mu_0\sigma_2}I_0(\theta_1^2\Delta)+\frac{1}{2}\frac{\nu^2\Delta}{\mu_0\sigma_2}I_2(\theta_1^2\Delta) & \frac{\nu^2\Delta}{\mu_0\sigma_1}I_1(\theta_2^1\Delta)-\frac{\nu^2\Delta}{\mu_0\sigma_1}I_3(\theta_2^1\Delta) & \frac{\nu^2\Delta}{\mu_0\sigma_2}I_1(\theta_2^2\Delta)-\frac{\nu^2\Delta}{\mu_0\sigma_2}I_3(\theta_2^2\Delta) \\
0 & 0 & 0 & 0 & 0 & 0 \\
0 & 0 & \frac{1}{2}\frac{\nu^2\Delta}{\mu_0\sigma_1}I_1(\theta_1^1\Delta)-\frac{1}{2}\frac{\nu^2\Delta}{\mu_0\sigma_1}I_3(\theta_1^1\Delta) & \frac{1}{2}\frac{\nu^2\Delta}{\mu_0\sigma_2}I_1(\theta_1^2\Delta)-\frac{1}{2}\frac{\nu^2\Delta}{\mu_0\sigma_2}I_3(\theta_1^2\Delta) & \frac{\nu^2\Delta}{\mu_0\sigma_1}I_0(\theta_2^1\Delta)-\frac{\nu^2\Delta}{\mu_0\sigma_1}I_4(\theta_2^1\Delta) & -\frac{\nu^2\Delta}{\mu_0\sigma_2}I_0(\theta_2^2\Delta)+\frac{\nu^2\Delta}{\mu_0\sigma_2}I_4(\theta_2^2\Delta) \\
0 & 0 & 0 & 0 & 0 & 0 \\
0 & 0 & -\frac{1}{2}\frac{\nu^2\Delta}{\mu_0\sigma_1}I_0(\theta_1^1\Delta)+\frac{\nu^2\Delta}{\mu_0\sigma_1}I_2(\theta_1^1\Delta)-\frac{1}{2}\frac{\nu^2\Delta}{\mu_0\sigma_1}I_4(\theta_1^1\Delta) & \frac{1}{2}\frac{\nu^2\Delta}{\mu_0\sigma_2}I_0(\theta_1^2\Delta)-\frac{\nu^2\Delta}{\mu_0\sigma_2}I_2(\theta_1^2\Delta)+\frac{1}{2}\frac{\nu^2\Delta}{\mu_0\sigma_2}I_4(\theta_1^2\Delta) & \frac{\nu^2\Delta}{\mu_0\sigma_1}I_3(\theta_2^1\Delta)-\frac{\nu^2\Delta}{\mu_0\sigma_1}I_5(\theta_2^1\Delta) & \frac{\nu^2\Delta}{\mu_0\sigma_2}I_3(\theta_2^2\Delta)-\frac{\nu^2\Delta}{\mu_0\sigma_2}I_5(\theta_2^2\Delta)
\end{pmatrix}
$$

Figure A1. Additional components to the original coefficient matrix of the TM-mode linear equation developed by Schwalenberg & Edwards [2004; Top of fig. 2 of Schwalenberg & Edwards (2004)]. As in fig. 2 of Schwalenberg & Edwards (2004), matrix components in the case where the maximum number of order n is 2 are shown. By adding these components to the TM-mode linear equation proposed by Schwalenberg & Edwards (2004), one can incorporate the contributions of the vertical electric field to the tangential electric field on the interface between the upper region and the lower region into the TM-mode linear equation.

electric component, instead of the tangential component, is continuous across the interface. We, therefore, modified the original TM-mode analytical formulation to take into account the contributions of the vertical electric field to the tangential electric field on the interface.

As shown in Schwalenberg & Edwards (2004), the tangential component of the electric field E_t on a sinusoidal seafloor is described as

$$E_t = E_x \cos(\psi) + E_z \sin(\psi) \tag{A1}$$

$$\psi = \arctan[-\nu\Delta\sin(\nu x)] \tag{A2}$$

where E_x and E_z are the horizontal and vertical electric field, respectively; Δ and ν are the amplitude and wavenumber of the sinusoidal seafloor, respectively. Since the tangential component E_t is continuous across the interface, E_t divided by $\cos(\psi)$, that is,

$$\frac{E_t}{\cos}(\psi) = E_x + E_z \tan(\psi) = E_x - E_z \nu\Delta\sin(\nu x), \tag{A3}$$

is also continuous across the interface. By placing superscripts 1 and 2 to the electric field components in the upper region and those in the lower region, respectively, as in Schwalenberg & Edwards (2004), the continuity of $E_t/\cos(\psi)$ on the interface between the two regions is described as

$$E_x^1 - E_z^1 \nu\Delta\sin(\nu x) = E_x^2 - E_z^2 \nu\Delta\sin(\nu x). \tag{A4}$$

This equation can be rearranged as

$$\left(E_x^1 - E_x^2\right) - \left(E_z^1 \nu\Delta\sin(\nu x) - E_z^2 \nu\Delta\sin(\nu x)\right) = 0. \tag{A5}$$

In the method proposed by Schwalenberg & Edwards (2004), in order to simplify the analytical formulation, the continuity of the horizontal electric component is assumed on the interface instead of eq. (A5);

$$E_x^1 - E_x^2 = 0. \tag{A6}$$

Schwalenberg & Edwards (2004) developed a linear equation [fig. 2 of Schwalenberg & Edwards (2004)] from eq. (A6) and an equation expressing the continuity of the magnetic field on the interface to obtain unknown coefficients $\beta_n \in \mathbb{C}$ (n = 0, ...) and $\gamma_n \in \mathbb{C}$ (n = 0, ...), which are defined in Schwalenberg & Edwards (2004). That is to say, of the two terms on the left-hand side of eq. (A5), only the first term is taken account into the TM-mode linear equation of Schwalenberg & Edwards (2004). By adding the contributions of the second term to the linear equation, one can construct the linear equation into which the contributions of E_z to E_t on the interface are incorporated.

From eqs (6), (7), (8) and (9) of Schwalenberg & Edwards (2004), the vertical component of the electric field on the interface is derived as

$$E_z^1 = -\frac{1}{\mu_0\sigma_1}\sum_{n=0}^{\infty} n\nu\beta_n \cdot e^{\theta_n^1\Delta\cos(\nu x)} \cdot \sin(n\nu x) \tag{A7}$$

$$E_z^2 = -\frac{1}{\mu_0\sigma_2}\sum_{n=0}^{\infty} n\nu\gamma_n \cdot e^{-\theta_n^2\Delta\cos(\nu x)} \cdot \sin(n\nu x). \tag{A8}$$

$$\theta_n^1 = \sqrt{i\omega\mu_0\sigma_1 + n^2\nu^2}, \tag{A9}$$

$$\theta_n^2 = \sqrt{i\omega\mu_0\sigma_2 + n^2\nu^2}, \tag{A10}$$

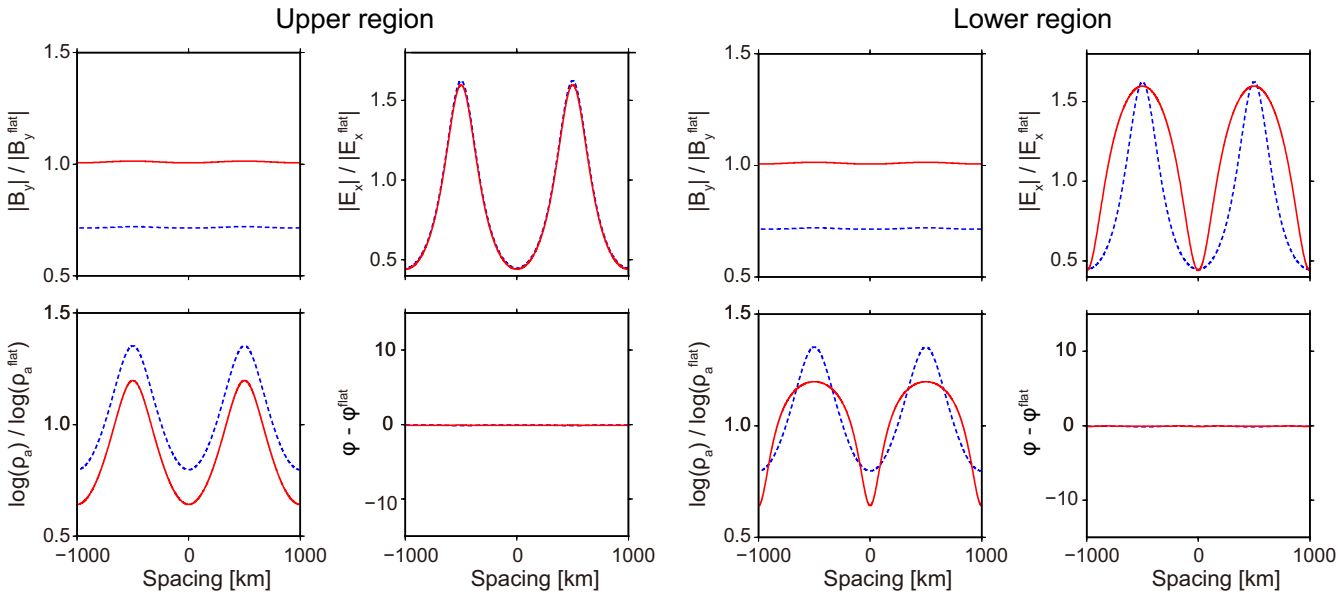

Figure A2. Horizontal EM field, apparent resistivity and phase of the TM mode calculated for a sinusoidal seafloor. These quantities are normalized by their respective values calculated from a flat interface. Red solid lines indicate the quantities obtained by the modified analytical formulation while blue broken lines indicate the quantities obtained by the original analytical formulation proposed by Schwalenberg & Edwards (2004). Input parameters are the ones written in table 1 of Schwalenberg & Edwards (2004) except the maximum number of order n. The maximum number of order n used in this work is 99 so as to calculate accurate analytical solutions.

where σ_1 and σ_2 are the electrical conductivities of the upper region and that of the lower region, respectively, μ_0 is the magnetic permeability of free space and ω is angular frequency of EM field. It should be noted that eqs (A7) and (A8) are different from eqs (15) and (16) of Schwalenberg & Edwards (2004). The first and second term of eq. (15) of Schwalenberg & Edwards (2004) and the first term of eq. (16) of the previous work correspond to the electric field on the interface generated by the change of the magnetic field B_y along the vertical direction. These terms should not be taken account into the derivation of the vertical electric field since it results only from the change of the magnetic field along the horizontal direction. As shown in Schwalenberg & Edwards (2004), exponent functions in eqs (A7) and (A8) can be expanded as

$$e^{\theta_n^1 \Delta \cos(\nu x)} = \sum_{k=0}^{\infty} (2 - \delta_{0k})\, I_k\left(\theta_n^1 \Delta\right)\, \cos\left(k\nu x\right) \tag{A11}$$

$$e^{-\theta_n^2 \Delta \cos(\nu x)} = \sum_{k=0}^{\infty} (-1)^k\, (2 - \delta_{0k})\, I_k\left(\theta_n^2 \Delta\right)\, \cos\left(k\nu x\right), \tag{A12}$$

where $I_k \in \mathbb{C}$ is modified Bessel function and δ_{0k} is the Kronecker delta. From eqs (A7), (A8), (A11) and (A12), we obtain

$$\begin{aligned} -E_z^1 \nu \Delta \sin\,(\nu x) = {} & \frac{\nu^2 \Delta}{\mu_0 \sigma_1} \sum_{n\,=\,0}^{\infty} n \beta_n \\ & \cdot \sin\left(n\nu x\right) \sum_{k\,=\,0}^{\infty} (2 - \delta_{0k})\, I_k\left(\theta_n^1 \Delta\right) \cos\left(k\nu x\right) \sin\left(\nu x\right) \end{aligned} \tag{A13}$$

$$\begin{aligned} -E_z^2 \nu \Delta \sin\,(\nu x) = {} & \frac{\nu^2 \Delta}{\mu_0 \sigma_2} \sum_{n\,=\,0}^{\infty} n \gamma_n \\ & \cdot \sin\left(n\nu x\right) \sum_{k\,=\,0}^{\infty} (-1)^k\, (2 - \delta_{0k})\, I_k\left(\theta_n^2 \Delta\right) \cos\left(k\nu x\right) \sin\left(\nu x\right). \end{aligned} \tag{A14}$$

With the aid of the product-to-sum identities of trigonometric functions, eqs (A13) and (A14) can be rearranged as

$$
\begin{aligned}
-E_z^1 \nu\Delta\sin(\nu x) = & -\frac{1}{4}\frac{\nu^2\Delta}{\mu_0\sigma_1}\sum_{n=0}^{\infty} n\beta_n \sum_{k=0}^{\infty}(2-\delta_{0k})\, I_k\left(\theta_n^1\Delta\right)\cos\left[(n+k+1)\,\nu x\right] \\
& +\frac{1}{4}\frac{\nu^2\Delta}{\mu_0\sigma_1}\sum_{n=0}^{\infty} n\beta_n \sum_{k=0}^{\infty}(2-\delta_{0k})\, I_k\left(\theta_n^1\Delta\right)\cos\left[(n+k-1)\,\nu x\right] \\
& -\frac{1}{4}\frac{\nu^2\Delta}{\mu_0\sigma_1}\sum_{n=0}^{\infty} n\beta_n \sum_{k=0}^{\infty}(2-\delta_{0k})\, I_k\left(\theta_n^1\Delta\right)\cos\left[(n-k+1)\,\nu x\right] \\
& +\frac{1}{4}\frac{\nu^2\Delta}{\mu_0\sigma_1}\sum_{n=0}^{\infty} n\beta_n \sum_{k=0}^{\infty}(2-\delta_{0k})\, I_k\left(\theta_n^1\Delta\right)\cos\left[(n-k-1)\,\nu x\right] \qquad \text{(A15)}
\end{aligned}
$$

$$
\begin{aligned}
-E_z^2 \nu\Delta\sin(\nu x) = & -\frac{1}{4}\frac{\nu^2\Delta}{\mu_0\sigma_2}\sum_{n=0}^{\infty} n\gamma_n \sum_{k=0}^{\infty}(-1)^k(2-\delta_{0k})\, I_k\left(\theta_n^2\Delta\right)\cos\left[(n+k+1)\,\nu x\right] \\
& +\frac{1}{4}\frac{\nu^2\Delta}{\mu_0\sigma_2}\sum_{n=0}^{\infty} n\gamma_n \sum_{k=0}^{\infty}(-1)^k(2-\delta_{0k})\, I_k\left(\theta_n^2\Delta\right)\cos\left[(n+k-1)\,\nu x\right] \\
& -\frac{1}{4}\frac{\nu^2\Delta}{\mu_0\sigma_2}\sum_{n=0}^{\infty} n\gamma_n \sum_{k=0}^{\infty}(-1)^k(2-\delta_{0k})\, I_k\left(\theta_n^2\Delta\right)\cos\left[(n-k+1)\,\nu x\right] \\
& +\frac{1}{4}\frac{\nu^2\Delta}{\mu_0\sigma_2}\sum_{n=0}^{\infty} n\gamma_n \sum_{k=0}^{\infty}(-1)^k(2-\delta_{0k})\, I_k\left(\theta_n^2\Delta\right)\cos\left[(n-k-1)\,\nu x\right]. \qquad \text{(A16)}
\end{aligned}
$$

In eqs (A15) and (A16), horizontal location x appears only in cosine functions as in eqs (21), (22) and (23) of Schwalenberg & Edwards (2004). Therefore, using eqs (A15) and (A16), the second term of eq. (A5) can be merged into the TM-mode linear equation of Schwalenberg & Edwards (2004), where cosine functions, which depend on the horizontal location x, are deleted after putting the terms including the same order of cosine function to the same row. Contributions of the second term of eq. (A5) to the TM-mode linear equation of Schwalenberg & Edwards (2004) is illustrated in Fig. A1, where additional components to the original coefficient matrix in the case where the maximum number of order n is 2 are shown. By adding these additional components to the original coefficient matrix, we obtain the linear equation into which the contributions of E_z to E_t on the interface are incorporated. Solving the linear equation, coefficients β_n $(n = 0, \ldots)$ and γ_n $(n = 0, \ldots)$ are obtained. By substituting these coefficients into eqs (26), (27), (28) and (29) of Schwalenberg & Edwards (2004), the horizontal components of electric field and magnetic field on the interface are calculated.

In Fig. A2, the horizontal EM field, apparent resistivity and phase for a sinusoidal seafloor calculated by the modified method are compared with the respective ones calculated by the original method proposed by Schwalenberg & Edwards (2004). These quantities are normalized by the respective ones calculated from a flat seafloor. Input parameters used in the calculation are the ones written in table 1 of Schwalenberg & Edwards (2004) except the maximum number of order n. In order to calculate accurate analytical solutions, the maximum number of order n used in this work is 99. Magnitude of the horizontal magnetic field for a sinusoidal seafloor obtained by the modified method is close to that for a flat seafloor, while magnitude of the horizontal magnetic field for a sinusoidal seafloor obtained by the original method is about 70 per cent of that for a flat seafloor. As a result, the apparent resistivity obtained by the modified method is about a half of that obtained by the original method in the upper region (i.e. above the seafloor). About phases, there is little difference between the two methods. In addition, when the modified method is used, the magnitude of the horizontal electric field in the upper region is significantly different from that in the lower region on seafloor slopes, leading to the significant difference between apparent resistivity in the upper region and that in the lower region.

APPENDIX B: BATHYMETRIC EFFECT OF THE MODEL USED IN SYNTHETIC INVERSION TEST

To evaluate the bathymetric effect of the model used in the synthetic inversion test of Section 2, impedance tensors and VMTFs were computed from the model with the bathymetry depicted in Fig. 4(a), but without anomalies. That is to say, its subsurface resistivity is uniformly 100 Ωm. For convenience, the response functions using the electric field perpendicular and parallel to the land–sea boundary are denoted hereinafter, respectively, as TM mode and TE mode, although the EM field of the model is 3-D. Figs B1 and B2, respectively, portray the maps of the apparent resistivity and the phase. Also, Fig. B3 shows induction arrows. At the land sites, the TM-mode apparent resistivity becomes higher than 100 Ωm (Fig. B1) and the TM-mode phase is lower than that for the case without bathymetry (Fig. B2). At some seafloor sites near the land–sea boundary, the TM-mode apparent resistivity becomes much lower than 100 Ωm. These features are known as the galvanic TM-mode coast effects (Constable *et al.* 2009; Key & Constable 2011). Furthermore, around the land–sea boundary, induction arrows tend to point towards the ocean (Fig. B3), which is also considered to be caused by the coast effects. It is noteworthy that, at 100 s, the magnitudes of the real arrows of the sites at $(x, y) = (-62.5, -12.5)$ and $(x, y) = (12.5, 62.5)$ are more than twice larger than the unit length. At the period,

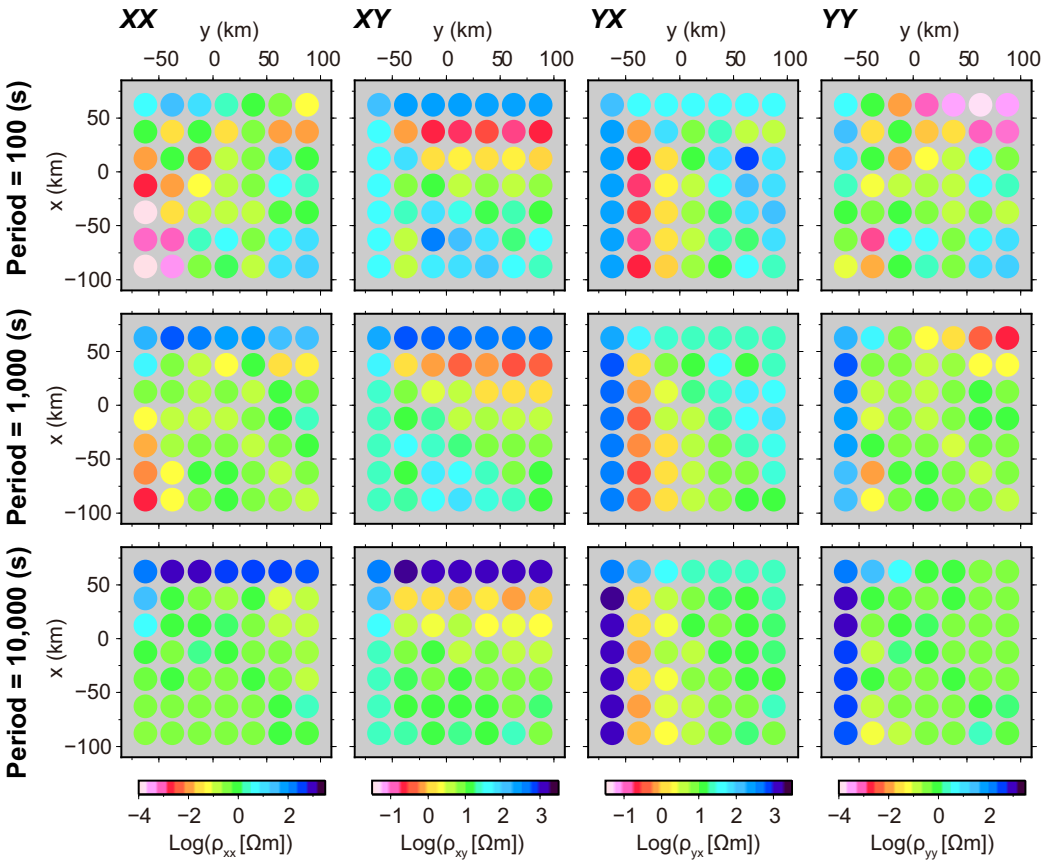

Figure B1. Maps of the apparent resistivity obtained from the 100 Ωm uniform Earth with the bathymetry described in Section 2.

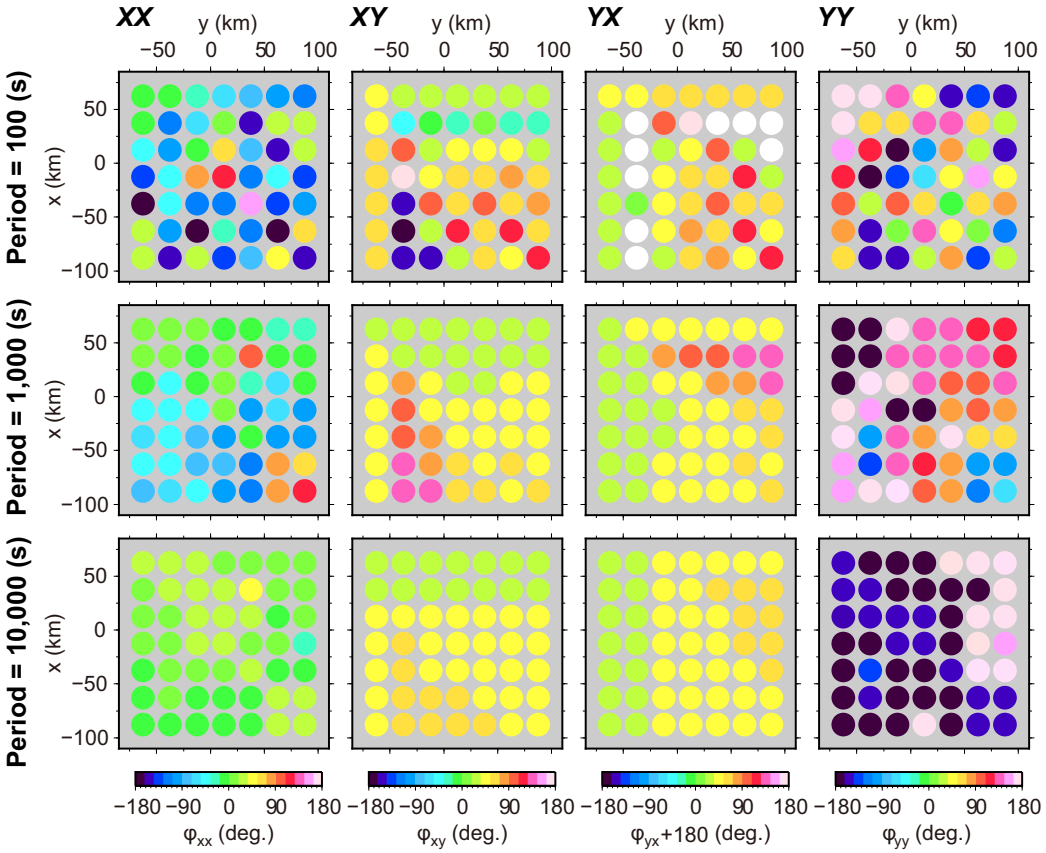

Figure B2. Maps of the phase obtained from the 100 Ωm uniform Earth with the bathymetry described in Section 2.

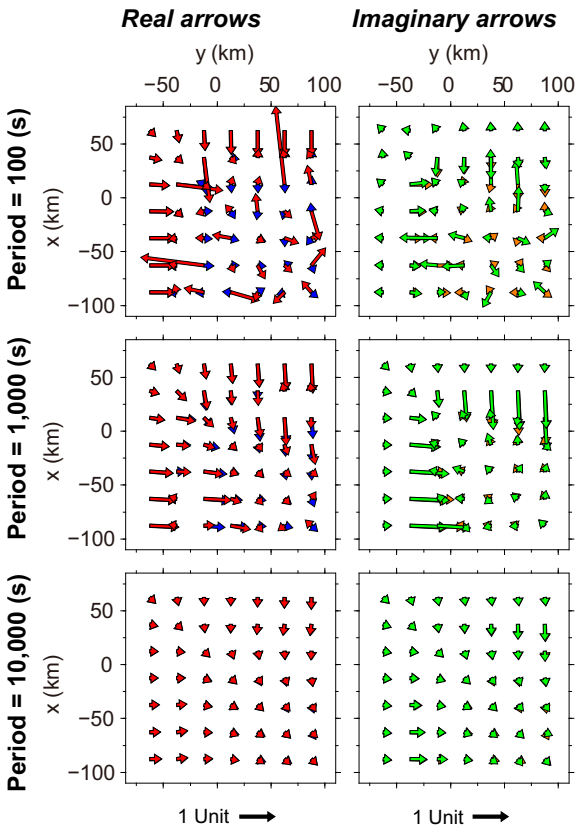

Figure B3. Maps of the induction arrows (Parkinson convention) obtained from the 100 Ωm uniform Earth with the bathymetry described in Section 2. Red and green arrows are calculated from the model with both the coast line and the seafloor undulations while blue and orange arrows are calculated from the model only with the coast line.

the TE-mode apparent resistivities at these points are about 1000 Ωm, which is an order of magnitude greater than that of the surroundings. In the sounding curves of those points, a positive peak was found at around 100 s in the TE-mode apparent resistivity. Such a peak in the TE-mode apparent resistivity and anomalously high tipper magnitude are identifying characteristics of the TE-mode coast effects (Key & Constable 2011; Worzewski *et al.* 2012). As documented in Key & Constable (2011) and Worzewski *et al.* (2012), the TE-mode coast effects are apparent at narrowed areas and a limited range of periods, whereas the TM-mode coast effects appear at wider areas and broader period ranges. In addition, on the seafloor, the apparent resistivity and phase do not vary smoothly in the space, and induction arrows at 100 s tend to point away from $(x, y) = (-40.0,\ 40.0)$. Since these features are not accounted for solely by the presence of the land–sea boundary (Fig. B3), they should be attributed to the seafloor undulations.